Lithogeochemistry, Geochronology and Geodynamic Setting of the Lupa Terrane, Tanzania: Implications for the Extent of the Archean Tanzanian Craton

Christopher J.M. Lawley[a†], David Selby[a], Daniel J. Condon[b], Matthew Horstwood[b], Ian Millar[b], Quentin Crowley[c], and Jonathan Imber[a]

[a]Department of Earth Sciences, Durham University, Science Labs, Durham, DH1 3LE, UK

[b]Natural Environment Research Council Isotope Geosciences Laboratory, British Geological Survey, Keyworth, Nottingham, NG12 5GG, UK

[c]School of Natural Sciences, Department of Geology, Trinity College, Dublin 2, Ireland

[†]corresponding author email: clawley@NRCan.gc.ca; tel: (613) 996-2593

Current Address: Natural Resources Canada, Geological Survey of Canada, 601 Booth Street, Ottawa, Ontario, K1A 0E8, Canada

Abstract

Hitherto, the Lupa Terrane, SW Tanzania is a poorly understood litho-tectonic terrane comprising the Paleoproterozoic Ubendian Belt. Herein we provide new U-Pb zircon ID-TIMS, U-Pb zircon LA-MC-ICP-MS and Lu-Hf zircon LA-MC-ICP-MS results from the Lupa Terrane and demonstrate that previously considered Paleoproterozoic granitoids are in fact Archean (ca. 2.74 Ga). Foliated Archean granitoids are in turn intruded by non-foliated and voluminous Paleoproterozoic granitic–gabbroic intrusions (1.96–1.88 Ma). Archean and Paleoprotoerozic intrusive phases possess trace element characteristics that are typical of volcanic arcs and the latter possess geochemical and field evidence for crust-magma interaction. New geochemical results and field relationships suggest that the Lupa Terrane was a continental margin during the Paleoproterozoic onto which the other Ubendian litho-tectonic terranes were accreted. Our model implies at least a 150 km SW extension of the currently accepted position of the Tanzanian cratonic margin. U-Pb zircon ages constrain Ubendian tectono-magmatic models and provide new evidence to support the protracted nature of the 1.9–1.8 Ga

Ubendian accretionary history. Lu-Hf zircon model ages provide evidence for ≥3.1 Ga crust underlying the Lupa Terrane that are consistent with some of the oldest ages reported for the Tanzanian Craton and previously reported seismic tomography studies that suggest significant portions of the Ubendian Belt represent re-worked Archean lithosphere.

Keywords: Lupa Terrane, Ubendian Belt, Usagaran Belt, Tanzanian Craton, Eburnian Orogeny, Paleoproterozoic

1 Introduction

Archean cratonic margins are complex geologic settings characterized by overprinting structural, magmatic, and metamorphic events (e.g., Zhoa et al., 2002; Reddy and Evans, 2009). This is particularly apparent in the Paleoproterozoic Ubendian and Usagaran metamorphic Belts which border the western and southern margins of the Tanzania Craton, respectively. Existing models for the Paleoproterozoic tectonic evolution of the Tanzanian cratonic margin invoke thrust-dominated accretion of terranes comprising the Usagaran Belt coupled with lateral accretion of terranes comprising the Ubendian Belt (Daly, 1988; Lenoir et al., 1994). However, recent geochronologic evidence suggests that the current configuration of the Ubendian Terranes is the product of at least three discrete orogenic events that are correlated to the Ubendian, Kibaran and Pan-African orogenic episodes (Boniface et al., 2012; Boniface and Schenk, 2012). The Paleoproterozoic tectonic history of the Ubendian Belt and the Tanzanian cratonic margin therefore remains poorly understood due, in part, to Neoproterozoic and Pan-African cover rocks, Meso- and Neoproterozoic metamorphic overprints, and periodic reactivation of geologic structures from the Paleoproterozoic until the present day (Theunissen et al., 1996).

The Lupa Terrane is located adjacent to the Tanzanian Craton and is the least-understood of the eight litho-tectonic terranes comprising the Ubendian Belt (Figs. 1–2; Daly, 1988). Voluminous granitoids intruding the Lupa Terrane that obscure the southern extent of the Tanzanian cratonic margin have, hitherto been attributed to widespread Paleoproterozoic magmatic activity related to the Ubendian Orogeny (e.g., Sommer et al., 2005). Herein we characterize and date these and other major lithologies in the Lupa Terrane and place constraints on the Paleoproterozoic geodynamic evolution of the Ubendian Belt. New U-Pb zircon LA-MC-ICP-MS ages, coupled with Lu-Hf zircon LA-MC-ICP-MS results, call into question the currently accepted SW extent of the Tanzanian cratonic margin (Manya, 2011). Establishing the extent of the Tanzanian Craton places important constraints on the prospectivity of SW Tanzania for ore deposits associated with Archean Cratons (e.g., orogenic Au deposits; Sango, 1988; Lawley, 2012).

2 Geologic Setting

2.1 Regional Geology

The western margin of the Tanzanian Craton is separated from the Congo Craton and the Bangweulu Block by the ca. 600 km long and 150 km wide zone of granulite-amphibolite facies meta-igneous and meta-sedimentary rocks known as the Ubendian Belt (McConnell, 1950; Sutton et al., 1954; Lenoir et al., 1994). Current tectonic models divide the Ubendian Belt into eight lithologicaly- and structurally-defined terranes: Ubende, Wakole, Katuma, Ufipa, Mbozi, Lupa, Upangwa, and Nyika (Fig. 1a; Daly, 1988). Mesoproterozoic meta-sedimentary rocks, corresponding to the Muva Supergroup, unconformably overlie the Ubendian Belt and have been subsequently metamorphosed during the Kibaran Orogeny (Cahen et al., 1984). These rocks are in turn overlain by Neoproterozoic clastic sedimentary rocks which correspond to the Bukoban Supergroup (Cahen et al., 1984). Meso- and Neoproterozoic cover sequences blanket large areas of the Ubendian basement and obscure its northern and southern limits (Hanson, 2003).

The Ubendian Belt formed through a series of metamorphic and tectonic events that span ca. 300 Myr (Lenoir et al., 1994). The first tectonic event is constrained by U-Pb zircon and Rb-Sr whole rock dating of syntectonic magmatic intrusions at 2093–2048 Ma (Dodson et al., 1975; Lenoir et al., 1994; Ring et al., 1997). The 2.1–2.0 Ga Ubendian tectonic phase corresponds with a period of eclogite and granulite facies metamorphism, the development of a ductile E-W trending tectonic fabric and is concomitant with metamorphism in the adjacent Usagaran Belt (Lenoir et al., 1994; Collins et al., 2004). Eclogitic rocks with MORB-like chemistry from the Usagaran, dated at ca. 2.0 Ga, suggest that metamorphism and tectonism resulted from subduction zone processes analogous to modern-day accretionary margins and may have resulted from the collision between the Tanzanian and Congo Cratons and the Bangweulu Block (Möller et al., 1995). Structural evidence associated with the 2.1–2.0 Ga Ubendian tectonic phase has largely been overprinted by later deformation, with the exception of the Mbozi Terrane (Theunissen et al., 1996).

The 2.1–2.0 Ga Ubendian tectonic phase is overprinted by a 1.9–1.8 Ga tectonic phase that produced the characteristic Terrane-bounding NW-SE trending shear zones and amphibolite facies metamorphism (Lenoir et al., 1994). The exact timing of this deformation event is poorly constrained and is thought to have occurred at 1860 ± 23 Ma based on a weighted average age of U-Pb and whole rock Rb-Sr ages of late-kinematic granitoids (Lenoir et al., 1994; Fig. 2). This age overlaps within analytical uncertainty with a weighted average Ar-Ar barroisite cooling age of 1848 ± 6 Ma from a mafic tectonite that is also interpreted to record the 1.9–1.8 Ga Ubendian tectonic phase (Boven et al., 1999), whereas the Kate Granite post-dates the second Ubendian tectonic phase and provides a possible maximum age for deformation at ca. 1825 Ma (Rb-Sr whole rock; Schandelmeier, 1983). These Rb-Sr and Ar-Ar ages are younger than recent U-Pb (SIMS) zircon dating of eclogites with MORB-like chemistry that suggest high-pressure and low-temperature metamorphism, analogous to modern-day subduction zones, occurred within the Ubende Terrane at 1886 ± 16 and 1866 ± 14 Ma (Boniface et al., 2012). Paleoproterozoic granites and tectonites are in turn overprinted during the Meso- and Neoproterozoic orogenic episodes (Theunissen et al., 1992; Ring et al., 1993; Ring et al., 1997; Theunissen et al., 1996). In particular, Paleo- and Neoproterozoic-aged eclogites with MORB-like chemistry represent paleo-sutures and suggest the current configuration of Ubendian Terranes is the result of at least three discrete orogenic cycles (Boniface, 2009; Boniface and Schenk, 2012). Our U-Pb ages place new geochronologic constraints on the timing of metamorphism, tectonism, and magmatism in the Lupa Terrane and provide new evidence to support the Ubendian Belt's protracted Paleoproterozoic tectonic evolution.

2.2 Local Geology

The geology of the Lupa Terrane has been variably described as comprising high-grade gneissic, high-grade schistose rocks, and granitic gneisses (e.g., Grantham, 1931, 1932, 1933; Teale et al., 1935; Gallagher, 1939; Harris, 1961; Van Straaten, 1984; Daly, 1988; Sango, 1988; Lenoir et al., 1994). The extent of the Lupa Terrane is also unclear from the literature (e.g., Kimambo, 1984; Daly, 1988). For the purposes of this study the Lupa Terrane is assumed to be coincident with the extent of the Lupa goldfield which is defined as the triangular shaped block bounded by the Rukwa Rift Escarpment (or Lupa Border Fault; Kilembe and Rosendahl, 1992) to the west, the Mkondo Magnetic Lineament to the north (Marobhe, 1989), and the Usangu Escarpment to the east. The Rukwa and Usangu Escarpments represent Tertiary faults that are related to the East African Rift, whereas the nature of the Mkondo Magnetic Lineament is more cryptic (Marobhe, 1989). The field area for the current study is located in the northern portion of the Lupa Terrane and corresponds with the mineral exploration licenses currently controlled by Helio Resource Corp. (Fig. 3). These mineral exploration licenses contain a number of orogenic gold systems and include the Kenge and Porcupine exploration targets (e.g., Lawley, 2012; Lawley et al., in press).

Hitherto geochronology of the Lupa Terrane has been limited to a K-Ar ages from a greisen and granite at 1802 ± 70 Ma and 1827 ± 70 (Cahen et al., 1984), respectively, and two poorly constrained U-Pb zircon ages of the Ilunga Granite (1931 ± 44 Ma; MSWD = 110; n = 4) and Saza Granite (1936 ± 47 Ma; MSWD = 230; n = 4; Mnali, 1999). Two SIMS U-Pb zircon ages of the Saza granite and a cross cutting mafic dike were also dated at 1924 ± 13 (MSWD = 2.6) and 1758 ± 33 Ma (MSWD = 0.9), receptively (Manya, 2012). The Ilunga and Saza granites intruded into what has been previously mapped as a "highly-deformed acid schist" (e.g., Kimambo, 1984) and "gneiss" (e.g., Grantham, 1932; Teale, 1935; van Straaten, 1984). We provide new geologic, geochemical evidence and geochronologic evidence to re-classify these rocks and propose a geodynamic setting to explain their occurrence.

3 Analytical Methods

3.1 U-Pb Zircon ID-TIMS

The detailed analytical methodology is presented in an electronic supplement, but is briefly summarized here. All of the analyzed zircon crystals have undergone the "chemical abrasion" (thermal annealing and subsequent leaching) pre-treatment technique (Mattinson, 2005) for the effective elimination of Pb-loss. Isotope ratios were measured at the NERC Isotope Geosciences Laboratory (NIGL), UK, using a Thermo-Electron Triton Thermal Ionisation Mass-Spectrometer (TIMS). Pb isotopes were measured by peak-hopping on a single SEM detector. U isotopic measurements were made in static Faraday mode. Age calculations and uncertainty estimation were based upon the algorithms of Schmitz and Schoene (2007).

3.2 U-Pb Zircon LA-MC-ICP-MS

This analytical methodology is also presented in detail in the electronic supplement but is briefly described here. Laser Ablation Multi-Collector Inductively Coupled Mass Spectrometry (LA-MC-ICP-MS) was completed at the NERC Isotope Geoscience Laboratory (NIGL). Zircon mineral separates were mounted in epoxy, polished, and imaged using cathodluminesence (CL) on a scanning electron microscope (SEM) at the British Geological Survey (BGS; except for CL098 which was prepared at the School of Natural Sciences, Trinity College Dublin). Zircon crystals were ablated using a New Wave Research Nd:YAG laser ablation system and isotopes ratios measured using a Nu Plasma MC-ICP-MS equipped with a multi-ion-counting array. The internationally recognized 91500 zircon standard (Weidenbeck et al., 1995) was used as the primary standard, whereas Plešovice (Sláma et al., 2008) and GJ-1 (Jackson et al., 2004) were used as secondary standards. All $^{206}Pb/^{238}U$ dates (ID-TIMS and LA-MC-ICP-MS) are calculated using the ^{238}U and ^{235}U decay constants of Jaffey et al. (Jaffey et al., 1971). The consensus value of $^{238}U/^{235}U = 137.818 \pm 0.045$ (Hiess et al., 2012) was used in the data reduction calculations for ID-TIMS and LA-MC-ICP-MS dates. Using this more accurate value with its associated uncertainty estimate has the effect of lowering $^{207}Pb/^{206}Pb$ dates at ca. 2 Ga by 0.8 ± 0.6 Myr, compared to $^{207}Pb/^{206}Pb$ dates calculated using the consensus value of $^{238}U/^{235}U = 137.88$.

3.3 Lu-Hf Zircon LA-MC-ICP-MS

Near concordant (>95% concordance) U-Pb zircon ablation sites from samples CL098, CL109, and CL1020 were re-analyzed to measure their respective Lu-Hf isotopic compositions. Isotope analyses were carried out at the NIGL using a Thermo Scientific Neptune Plus MC-ICP-MS coupled to a New Wave Research UP193FX excimer laser ablation system and low-volume ablation cell. Helium was used as the carrier gas through the ablation cell with Ar make-up gas being connected via a T-piece and sourced from a Cetac Aridus II desolvating nebulizer. After initial set-up and tuning a 2% HNO_3 solution was aspirated during the ablation analyses. Lutetium (^{175}Lu), ytterbium (^{172}Yb, ^{173}Yb), and hafnium (^{177}Hf, ^{178}Hf, ^{179}Hf, and ^{180}Hf) isotopes were measured simultaneously during static 30s ablation analyses (50 µm; fluence = 8–10 J/cm^2). A standard–sample–standard bracketing technique, using reference zircon 91500, was used to monitor accuracy of internally corrected Hf isotope ratios and instrumental drift with respect to the Lu/Hf ratio. Hf reference solution JMC475 was analyzed during the analytical session to allow normalisation of the laser ablation Hf isotope data. Correction for ^{176}Yb on the ^{176}Hf peak was made using reverse-mass-bias correction of the $^{176}Yb/^{173}Yb$ ratio (0.7941) empirically derived using Hf mass bias corrected Yb-doped JMC475 solutions (cf. Nowell & Parrish, 2001). ^{176}Lu interference on the ^{176}Hf peak was corrected by using the measured ^{175}Lu and assuming $^{176}Lu/^{175}Lu = 0.02653$.

3.4 Lithogeochemistry

A representative suite (23 samples) of magmatic phases were analyzed for major and trace elements using a combination of fusion inductively coupled plasma-mass spectrometry (ICP-MS) and instrumental neutron activation analysis (INAA) by Actlabs (Ancaster, Ontario; method 4E-Research). Sample aliquants for ICP-MS analysis were first mixed with a lithium metaborate-tetraborate flux and fused in order to ensure complete digestion of refractory minerals (e.g., zircon). As a result, fusion ICP-MS results are considered most representative and are used for plotting purposes. Detection limits for this assay package are in the low ppm and ppb range for most trace elements. Standards, duplicates and blanks were used as a means of quality control and the difference between duplicate analyses were generally within a few ppm for most trace elements.

4 Results and Data Interpretation

4.1 Lithologies

All rocks within the field area have undergone hydrothermal alteration and greenschist facies metamorphism. Thus, all rock names are metamorphic and for the remaining discussion all rock names should have the prefix "meta-" (Figs. 4–6). Non-foliated felsic-mafic magmatic rocks intrude into a pervasively deformed granitic unit (Figs. 4a, b, and c). Rocks lacking this pervasive tectonic fabric have been classified according to the IUGS classification scheme (LeMaitre, 2002). Two granitoids, the Saza Granodiorite and Ilunga Syenogranite (named after their outcrop localities adjacent to the town of Saza and the Ilunga Hills, respectively), are exceptions and their IUGS names are accompanied by the prefix Saza and Ilunga, respectively as a result of their regional significance (Fig. 3). Intermediate and mafic rocks are difficult to classify using the IUGS scheme because the primary mineralogy has been partially to completely replaced by amphibole (± relict pyroxene) and plagioclase (Fig. 6c). The large range of amphibole content (modes 15–60%) coupled with the large range of SiO_2 (50–60% SiO_2; see below) and Mg# (44–73; see below) suggests these rocks represent a compositional spectrum of protoliths (discussed further below). As a result, amphibole-plagioclase rocks are termed the diorite-gabbro suite in the following lithogeochemistry discussion (Mnali, 2002). Sample locations, descriptions, and modal mineralogy are presented in Table 1.

Foliated granitoids crop out in the southern portion of the field area (Fig. 3). K feldspar, quartz and plagioclase are the dominant mineral assemblage with lesser amounts of chlorite ± calcite ± titanite ± epidote. However, foliated granitoids exhibit a wide range of modal mineralogy (e.g., the modal mineralogy of foliated granitoids ranges from syenogranite to monzogranite) and likely represent several different lithologies, but have been grouped based on a distinct deformation fabric that is absent in the other identified granitoids. This characteristic foliation is defined by alternating quartz-feldspar and chlorite rich bands, which gives the rock a banded to "gneissic" appearance (Fig. 4b). Compositional banding is accompanied by crystal plastic deformation of quartz (Lawley et al., in press) and both characteristics are dissimilar to the mineralogy and deformation processes that are typical of gneissic rocks comprising the other Ubendian Terranes (Lenoir et al., 1994). Non-foliated granitoids, dioritic-gabbroic intrusions/dikes and aplitic dikes are all observed cross cutting foliated granitoids and suggest that fabric development occurred prior to widespread magmatism in the field area (Fig. 4c; Lawley et al., in press).

The Ilunga Syenogranite represents the dominant lithology in the northern portion of the field area and corresponds with a topographic high referred to as the Ilunga Hills (Fig. 3). K feldspar, quartz and plagioclase comprise the primary mineral assemblage with lesser amounts of chloritized biotite (typically less than 10% modal abundance). The Ilunga Syenogranite is typically equigranular and coarse grained, but locally grades into finer grained and more K feldspar rich zones with aplitic texture. The finer grain size and change in modal mineralogy is also accompanied with quartz-feldspar intergrowths in thin section (Fig. 6f). K feldspar-plagioclase intergrowths are also locally observed in thin section and are unique to the Ilunga Syenogranite within the field area. Very few igneous contacts between the Ilunga Syenogranite and other lithologies were observed aside from cross cutting diorite-gabbroic intrusions at the top of the Ilunga Hills, which coupled with mafic enclaves suggests diorite-gabbroic intrusions/dikes pre- and post-date the Ilunga Syenogranite.

The regionally significant Saza Granodiorite crops out in the southern portion of the field area as a coarse grained and equigranular intrusion (Fig. 3). Quartz, plagioclase and K feldspar comprise the dominant mineral assemblage with lesser amounts of chloritized biotite and hornblende (Fe-Mg minerals generally constitute less than 5% modal abundance). Sericite, calcite and epidote are also observed overprinting the primary mineral assemblage. Abundant diorite-gabbroic enclaves/xenoliths, coupled with cross cutting dioritic-gabbroic dikes/intrusions, suggests that the Saza Granodiorite was pre- and post-dated by dioritic-gabbroic magmatism (Fig. 5e). The Saza Granodiorite is also cross cut by auriferous mylonitic shear zones and aplite dikes (Fig. 3).

Dioritic-gabbroic dikes and intrusions represent a significant proportion of the rocks exposed in the field area and are typically observed cross cutting and intruding granitoids (Fig. 3). Amphibole and plagioclase are the dominant minerals, whereas chlorite, epidote, titanite and calcite are typically present as accessory phases (Fig. 6c). Rare relict pyroxene crystals are also observed and are variably altered by a chlorite ± epidote ± titanite ± calcite alteration assemblage. The presence of diorite-gabbroic enclaves/xenoliths in all of the identified and temporally distinct granitoids (discussed further below) is consistent with multiple dioritic-gabbroic intrusive events.

A variety of other granitoids, ranging from syenogranite to tonalite in modal mineralogy, were also observed in the field area and occur as dikes and small intrusions (Fig. 3). These additional non-foliated magmatic phases are observed cross cutting foliated granitoids, but are in turn cross cut by auriferous shear zones. Several of these magmatic phases remain undated (e.g., syenogranite; Fig. 3), however we expect that the majority of igneous activity occurred prior to mylonitization that is constrained by Re-Os sulphide ages at 1.88 Ga (Lawley et al., in press).

4.2 U-Pb Zircon ID-TIMS Results

For the detailed U-Pb zircon results see the Online Supplementary Table S1 and Fig. 7. Our interpreted crystallization ages are reported in Table 2 and were calculated using Isoplot v. 4.15 (Ludwig, 2008). The preferred crystallization age for each of the three samples is a weighted average $^{207}Pb/^{206}Pb$ age of concordant analyses because these zircon crystals exhibit the least evidence of disturbance and are the most likely to record crystallization ages. Sample CL0972 is a zircon mineral separate from the Ilunga Syenogranite that hosts the Porcupine ore body. Concordant zircon crystals from CL0972 yield a weighted average $^{207}Pb/^{206}Pb$ age of 1959.6 ± 1.0 (MSWD = 1.4; n = 5). Sample CL0975 is a zircon mineral separate from the Saza Granodiorite. Concordant zircon crystals from this sample yield a weighted average $^{207}Pb/^{206}Pb$ age of 1934.5 ± 1.0 (MSWD = 1.7; n = 5). Sample CL0911 is a zircon mineral separate from a non-foliated granodiorite dike that is observed cross cutting the foliated granitoid at the Kenge ore body (CL098 dated by LA-MC-ICP-MS; Fig. 4c). Concordant zircon crystals from sample CL0911 yield a weighted average $^{207}Pb/^{206}Pb$ age of 1958.5 ± 1.3 (MSWD = 0.41; n = 2), consistent with the less precise upper intercept date of 1964.6 ± 5.4 (MSWD = 3.6; n = 5). The lower intercept age of 1126 ± 150 Ma (MSWD = 3.6; n = 5) could represent a Pb-loss event during the Mesoproterozoic that is consistent with the timing of the Kibaran Orogeny (Boniface et al., 2012). In addition to determining the crystallization age of CL0911, U-Pb ages also constrain the maximum age of deformation for CL098 (see section 4.5).

4.3 U-Pb Zircon LA-MC-ICP-MS Results

All Cathodoluminesence (CL) images and ablation spot locations are provided as Online Supplementary Figures (see Online Supplementary Figs. S1–S6). Reference material analyses and sample results are provided as Online Supplementary Tables (see Online Supplementary Tables S2–S7). Data are presented on Concordia plots in Figures 9 and 10. Our preferred crystallization ages are reported in Table 2 and were calculated using Isoplot v. 4.15 (Ludwig, 2008). All zircon grains possess euhedral crystal shapes and complex magmatic oscillatory zoning characterized by truncated and resorbed growth phases. Zircon recrystallization is also suspected in weakly luminescent zircon zones that lack oscillatory zoning (Fig. 8).

Sample CL098 is a foliated granitoid that hosts the Kenge Au ore body. Twenty-six ablation analyses were measured from seventeen zircon crystals. Two of these analyses (zircon crystals 12-1 and 18-2) possessed significant common lead (1.7–3.8% f^{206}Pbc) and are therefore not shown in Figs. 9a, b. We consider the fifteen concordant (100 ± 2% concordance) analyses to reflect the best determination of the actual crystallization age of the sample and yield a weighted average ^{207}Pb/^{206}Pb age of 2723 ± 10 Ma (± 40 2 SD; MSWD = 5.8; n = 17). The large MSWD implies the assigned analytical uncertainties do not account for the observed U-Pb age range. Therefore, our dataset likely contains multiple zircon populations that possess similar but distinct ages that partially overlap within analytical uncertainty of individual analyses.

Sample CL109 is a foliated granitoid with a well-developed S- and L-fabric. Thirty-seven ablation spots from seventeen zircon crystals were analyzed. The majority of imaged zircon crystals from CL109 possess a bright and very-narrow rim that was not possible to analyse with a 25 µm spot size (Fig. 9a). Three of these zircon crystals (zircon crystals C5-1, C6-1, and H1-2) possess significant common lead (1.5–1.8% f^{206}Pbc) and are not shown in Figs. 9a, b. The remaining zircon crystals constrain a Model-2 York fit regression with an upper intercept age of 2754 ±14 Ma and lower intercept age at 512 ± 140 Ma (MSWD = 16; n = 34). The large MSWD reflects considerable scatter along the discordia curve and is indicative of complex and non-zero Pb-loss. The youngest ^{207}Pb/^{206}Pb ages correspond to what appear from CL images to be recrystallized zircon crystals; however several of the younger ^{207}Pb/^{206}Pb ages correspond with magmatically zoned and pristine portions of the zircon crystals. One of these analyses (J2-1) overlaps multiple growth zones, corresponds to a brightly-luminescent margin of the zircon, and possesses an anomalously low ^{207}Pb/^{206}Pb age at 2620 ± 17 Ma. If this analysis is excluded, a weighted average ^{207}Pb/^{206}Pb age for the remaining most concordant zircon crystals (>98% concordance) is 2758 ± 9 Ma (± 28 2SD; MSWD = 2.8; n = 11). The weighted average possesses a MSWD >1 and we interpret this to reflect multiple zircon populations included within the weighted average calculation.

Sample CL1020 is a foliated granitoid with a weakly developed tectonic fabric. Fifty-two ablation analyses were measured from eighteen zircon crystals. Seven of these analyses (G2-1, G2-2, C5-1, H9-1, I1-2, Z4-1, and Z7 2) possessed significant common lead (1.5–4.6% f^{206}Pbc) and are not shown in Figs. 9a, b. Concordant ^{207}Pb/^{206}Pb ages (>95% concordance) possess a 150 Myr age range that likely reflects at least two disparate age components and each has likely undergone non-zero Pb-loss. CL imaging provides textural support for an inherited zircon component with the oldest zircon crystals corresponding to highly luminescent and resorbed zircon cores (Fig. 8c). The age of this older population is unclear as inherited zircon crystals are suspected to have undergone non-zero Pb-loss, however a weighted average ^{207}Pb/^{206}Pb age of the five oldest and most concordant (100 ± 2% concordance) zircon crystals that correspond to texturally distinct zircon zones represents a minimum age estimate of inherited zircon crystals at 2846 ± 7 (± 9 2SD; MSWD = 0.31; n = 5). The crystallization age of CL1020 is similarly open to interpretation as the younger age population likely includes inherited zircon crystals that have undergone non-zero Pb-loss; however a weighted average ^{207}Pb/^{206}Pb age of the fourteen most concordant (100 ± 2% concordance) zircon crystals corresponding to magmatically zoned zircon crystals provides our best estimate for the crystallization age of CL1020 at 2739 ± 10 (± 35 2SD; MSWD = 4.6; n = 14).

Sample CL1019 is a porphyritic monzogranite and possesses K-feldspar megacrysts (locally several cm in diameter) that distinguish this lithology from the other granitic phases in the field. Thirty-two ablations from sixteen zircon crystals were analyzed. Seven of these analyses (A10-1; B3-1; B10-1; C1-1; C4-1; E2-1; G10-1) contained significant concentrations of common Pb (1.9–2.7% f^{206}Pbc) and are not included in Figs. 10a, b. Two of the remaining twenty-five analyses are from zircon G1 and possess significantly older U-Pb ages (ca. 700 Myr). One of these analyses is near-concordant (96% concordance) and provides a ^{207}Pb/^{206}Pb age of 2671 ± 17 Ma. This zircon possesses a resorbed and highly luminescent centre and weakly luminescent margin. The textural and isotopic evidence suggest that this zircon is consistent with an inherited zircon component that was derived from Archean basement (e.g., CL098, CL109, and CL1020). All other CL1019 zircon analyses possess Proterozoic U-Pb ages and constrain a Model-2 York fit regression with an upper intercept age of 1948 ± 16 Ma and lower intercept age of 87 ± 150 Ma (MSWD = 13; n = 23). The high

MSWD reflects significant scatter about the discordia curve that is likely related to Pb-loss and a range of concordant U-Pb ages that may suggest multiple zircon populations were included in the regression. Concordant analyses are most likely to reflect the true crystallization age of the sample, and a weighted average $^{207}Pb/^{206}Pb$ age of the most concordant (>98% concordance) and Proterozoic zircon crystals is 1942 ± 14 Ma (± 35 2SD; MSWD = 3.3; n = 8).

Sample CL1021 is a quartz diorite intrusion adjacent to the Saza granodiorite (CL0975). Thirty ablation spots were analysed from 14 zircon grains. Three of these analyses (J1-23, J1-24, and D9-16) possessed large counts of common lead (1.5–2.1% $f^{206}Pbc$) and are not presented in the concordia plots (Figs. 10a, b) or discussed further. The remaining zircon crystals constrain a Model-2 York fit regression with an upper intercept age of 1907 ± 27 Ma and lower intercept age of 524 ± 140 Ma (MSWD = 5.8; n = 27). The dataset likely contains multiple zircon populations that are unresolvable within the assigned analytical uncertainties based on the 107 Myr range of near-concordant (>95% concordance) $^{206}Pb/^{238}U$ ages coupled with the high MSWD of the upper intercept age (Fig. 10b). Our best approximation to the crystallization of CL1021 is the upper intercept age of all the analyzed zircon crystals (except for those with excessive common lead and analysis J1-25 which plots significantly below discordia) at 1891 ± 17 (2SD = ?, MSWD = 4.8; n = 26).

Sample CL1022 is a massive gabbroic dike that is observed cross cutting a foliated granitoid (CL109). Twenty-one ablation spots from ten zircon crystals were analyzed and constrain a Model-2 York fit regression with an upper intercept age at 1880 ± 17 Ma and lower intercept at age 469 ± 81 Ma (MSWD = 4.9; n = 21). Near-concordant (>95% concordant) zircon crystals possess a 160 Myr range of $^{206}Pb/^{238}U$ ages and imply our dataset contain multiple zircon populations (Fig. 10b). Our best approximation of the crystallization age of CL1022 is the upper intercept age of all analyzed zircon crystals at 1880 ± 17 Ma (2SD = X, MSWD = 4.9; n = 21). Our interpreted crystallization age also constrains the timing of crystallization and provides a maximum possible age for deformation within the foliated granitoid (CL109).

4.4 LA-MC-ICP-MS Lu-Hf Zircon Results

Three Archean foliated granitoid samples (CL098, CL109 and CL1020) were selected for LA-MC-ICP-MS Lu-Hf isotopic analysis. These samples were chosen because of their unexpected

Archean age and their poorly constrained petrogenetic history. Only near-concordant (>95% concordance) zircon analyses were selected for Lu-Hf analysis and, in the majority of cases, the Lu-Hf ablation sites were centred over top of the pre-existing U-Pb ablation site (e.g., Fig. 8c). For zircon crystals where this was not possible (e.g., zircon growth zones were too thin), the Lu-Hf ablation site was repositioned adjacent to the U-Pb ablation site in what is assumed to be a coeval growth zone of the zircon. For ablation sites and CL images see Online Supplementary Figs. S1, S2 and S4. Reference material analyses and sample results are provided as Online Supplementary Table S8.

Zircon crystals incorporate a small amount of ^{176}Lu during crystallization which decays to ^{176}Hf. As a result, each measured $^{176}Hf/^{177}Hf$ ratio needs to be corrected for the interpreted crystallization age of the sample ($^{176}Hf/^{177}Hf_{initial}$). We approached this problem by using the $^{207}Pb/^{206}Pb$ age of the ablation site and the measured $^{176}Lu/^{177}Hf$ ratios to correct for the corresponding $^{176}Hf/^{177}Hf$ analysis. Normalizing $^{176}Hf/^{177}Hf_{initial}$ ratios to the $^{176}Hf/^{177}Hf$ value of the present-day bulk earth ($^{176}Hf/^{177}Hf_p = 0.28295$; Patchett and Tatsumoto, 1980) allows the calculation of εHf [($^{176}Hf/^{177}Hf_{initial}$ / $^{176}Hf/^{177}Hf_{present\ day\ earth}$) x 10^4]. Crustal residence ages were calculated following a 2-stage model age approach. The calculated $^{176}Hf/^{177}Hf_{initial}$ ratio of the zircon at the time of growth ($^{207}Pb/^{206}Pb$ zircon age), and an average crustal $^{176}Lu/^{177}Hf$ ratio of 0.012 (Vervoort et al., 1999) were used to project back to the time of intersection with depleted mantle (with $^{176}Lu/^{177}Hf = 0.0384$, $^{176}Hf/^{177}Hf = 0.28325$: Chauvel and Blichert-Toft, 2001).

Forty-two Lu-Hf analyses were performed on fourteen zircon crystals from sample CL1020 (Fig. 11a). The $^{176}Hf/^{177}Hf$ analyses possess an approximately normal distribution and overlap within analytical uncertainty at the 2σ uncertainty level. Inherited zircon crystals possess identical $^{176}Hf/^{177}Hf_{initial}$ values (arithmetic average = 0.281010 ± 0.000045 at 2SD, n =26) within uncertainty but are generally lower than zircon crystals that are thought to represent crystallization of CL1020 at ca. 2.74 Ga (arithmetic average = 0.281032 ± 0.000029 at 2SD, n = 16).

Nineteen Lu-Hf analyses were performed on twelve concordant zircon crystals from CL098. $^{176}Hf/^{177}Hf$ analyses possess an approximately normal distribution and largely overlap within analytical uncertainty at the 2σ uncertainty level (Fig. 11a). An arithmetic average of $^{176}Hf/^{177}Hf_{initial}$ for this sample is 0.281048 ± 0.000046 (2SD, n =19).

Fifteen Lu-Hf analyses were performed on ten concordant zircon crystals from CL109. One Lu-Hf analysis (H1-2) possesses an anomalously low $^{176}Hf/^{177}Hf$. The significance of this value is unclear and is not included in the following discussion, but is include on Figure 11. The remaining $^{176}Hf/^{177}Hf$ analyses possess a weakly bi-modal distribution (Fig. 11a). $^{176}Hf/^{177}Hf_{initial}$ values are largely within analytical uncertainty of each other (arithmetic average = 0.281047 ± 0.000025 at 2SD, n = 14) and the $^{176}Hf/^{177}Hf_{initial}$ values of CL098 (i.e., 0.281048) and CL1020 (i.e., 0.281032). The four oldest U-Pb analyses possess the highest $^{176}Hf/^{177}Hf_{initial}$ values and overlap with $^{176}Hf/^{177}Hf_{initial}$ values of interpreted inherited zircon cores from CL1020 at the 2σ uncertainty level.

4.5 Interpretation of complex inheritance, recrystallization, and Pb-loss systematics

Concordant LA-MC-ICP-MS U-Pb zircon analyses possess age ranges that exceed the analytical uncertainty of the individual measurements (e.g., near-concordant zircon crystals from CL1022 possess a 160 Myr range; Figs. 9 and 10). Reference material analyses, run as part of our standard-sample-standard bracketing protocol, overlap within analytical uncertainty and suggest that our analytical methodology cannot explain this age range and that real geologic scatter exists in our samples. The cause of the concordant U-Pb zircon age range can be constrained by integrating the U-Pb and Lu-Hf analyses with CL imaging for the same ablation pits. Previous studies provide empirical evidence to suggest that the U-Pb and Lu-Hf isotopic systems are decoupled during metamorphism (e.g., Gerdes and Zeh, 2009; Kemp et al., 2009; Whitehouse and Kemp, 2010). As a result, the $^{176}Hf/^{177}Hf_{initial}$ remains unchanged even for zircon crystals that exhibit U-Pb evidence for Pb-loss. The oldest $^{207}Pb/^{206}Pb$ ages from CL1020 correspond to highly luminescent and resorbed zircon cores that are interpreted to be inherited xenocrysts. Lu-Hf isotopic data supports this interpretation as $^{207}Pb/^{206}Pb$ ages <2.74 Ga possesses $^{176}Hf/^{177}Hf_{initial}$ ratios identical to zircon crystals with $^{207}Pb/^{206}Pb$ ages at ca. 2740 Ma, whereas inherited zircon crystals with $^{207}Pb/^{206}Pb$ ages >2.74 Ga possess generally less radiogenic $^{176}Hf/^{177}Hf_{inititial}$ ratios. Our results possess considerable overlap, but generally less radiogenic, $^{176}Hf/^{177}Hf_{initial}$ values of inherited and magmatic zircon crystals suggest the source of inherited zircon crystals may have had a dissimilar Lu-Hf composition compared to the source of magmatic zircon crystals. Conversely, younger zircon crystals that possess identical $^{176}Hf/^{177}Hf_{initial}$ ratios have likely undergone non-zero Pb-loss.

4.6 Lithogeochemistry Results

For lithogeochemical results see Online Supplementary Table S9 and Figures 13–15. Several samples (e.g., CL0956, CL0922) possess major element concentrations that total to less than 100%, which suggests some element(s) are not accounted for in the total calculations. Part of this discrepancy is explained by sulphur bearing phases (e.g., pyrite) that are not included in the major element total calculations and/or suggests that unanalysed elements (e.g., C) may also be present as minor components within several samples. Hydrothermal alteration and greenschist facies metamorphism are ubiquitous features of Lupa Terrane lithologies. Petrographic evidence such as partial to complete replacement of feldspars with sericite (± calcite) and partial to complete replacement of Fe-Mg minerals with amphibole (± chlorite, ± epidote, ± clinozoisite, ± titanite, ± calcite, ± opaques) are indicative of pervasive hydrothermal circulation (Fig. 6c). Chemical alteration is also inferred from large variations in certain major elements and Large Ion Lithophile Elements (LILE) which are considered to be mobile during hydrothermal alteration and metamorphism (e.g., Cs, Rb, Ba, Sr, and Pb; Grant, 2005). High Field Strength Elements (HFSE; e.g., Ti, Zr, Y, Nb, Hf, Ta, U, and Th), transitional elements (e.g., Ni, Cr, V, and Sc), and Rare Earth Elements (REE; e.g., La, Ce, Pr, Nd, Sm, Eu, Gd, Tb, Dy, Ho, Er, Tm, Yb, Lu) are least disturbed by hydrothermal processes (Floyd and Winchester, 1975; Winchester and Floyd, 1977). Thus, the following discussion is focused on trace elements that are considered to be more representative of protolith composition.

The trace element composition of the felsic lithologies can be qualitatively divided into three REE patterns and all phases share similar trace element patterns normalized to primitive mantle (Fig. 13a). Saza Granodiorite (CL1030; CL0975), granodiorite samples (CL0911; CL0921; CL0958), and porphyritic monzogranite (CL1029) possess Light Rare Earth Element (LREE) enrichment (La/Sm_{CN} = 5.2–11.7) and concave-up trends in the Medium and Heavy Rare Earth Elements (MREE and HREE, respectively). This pattern is in contrast to the REE pattern of foliated granite samples (CL098; CL0925; CL0947) which possess LREE enrichment (La/Sm_{CN} = 3.8–8.1), steeply dipping patterns towards the HREE (La/Yb_{CN} = 20.9–64.6), and minor negative Eu anomalies (Eu/Eu* = 0.7–

0.9). The third qualitatively distinct REE pattern is shown by the Ilunga Syenogranite (CL0931; CL0932; CL0934; CL0959) which exhibits LREE enrichment (La/Sm_{CN} = 2.9–5.3), deep negative Eu anomalies (Eu/Eu* = 0.08–0.36), and flat MREE and HREE patterns (Gd/Yb_{CN} = 0.9–1.3). On trace element plots normalized to primitive mantle, all felsic phases possess LILE enrichment, gently-dipping patterns towards the REE, and are characterized by large negative Nb and Ti anomalies (Nb/Th_{CN} = 0.1–0.6; Ti/Sm_{CN} = 0.0–0.3; Fig. 13b).

The trace element compositions of the intermediate and mafic magmatic phases can be qualitatively divided into two trace element groups (Figs. 13c and d). The diorite-gabbro suite (CL1021; CL1022; CL0913; CL0923; CL0928; CL0957; CL0981; CL0984) possess LREE enrichment (La/Sm_{CN} = 2.1–4.0) and gently-dipping slopes towards the HREE (La/Yb_{CN} = 3.0–19.9) and minor positive Eu (i.e., Eu/Eu* = 1.5–1.1) anomalies. This distinctive REE profile is complimented by LILE enrichment relative to HFSE, large negative Nb anomalies (Nb/Th_{CN} = 0.1–0.2), and small negative Ti anomalies (Ti/Sm_{CN} = 0.2–1.2; only CL1022 has a positive Ti anomaly). Two samples, CL0956 and CL0996, are dikes that cross cut foliated granitoids and the diorite-gabbro suite, respectively and preserve their original clinopyroxene and orthopyroxene mineralogy. This suggests that these two dikes post-date greenschist facies metamorphism and are potentially the youngest rocks in the field area. These samples do not possess negative Nb or Ti anomalies which is a consistent pattern shown by all other igneous phases in the sample suite. In addition, sample CL0956 possess an alkaline major element chemistry (K_2O wt. % + Na_2O wt. % = 6 % at 50 wt. % SiO_2), which contrasts with the calc-alkaline nature of all the other magmatic phases. The timing and petrogenetic significance of these late dikes is unclear.

4.7 REE Modelling

Our REE modelling used the non-modal melting equation of Shaw (1970) to assess whether the diorite-gabbro suite could have formed from mantle sources with compositions typical of volcanic arcs (following the approach of Dampare et al., 2008; Fig. 14). We chose primitive mantle (PM; Sun and McDonough, 1989) and the depleted mid-ocean ridge basalt (DMM; McKenzie and O'Nions, 1991) as starting compositions and then calculated the REE concentrations of melts at increasing degrees of partial melting. N-MORB and E-MORB (Sun and McDonough, 1989) are also plotted for reference. Mineral/matrix partition coefficients are from McKenzie and O'Nions (1991); whereas mineral modes and melt-modes for garnet lherzolite and spinel lherzolite are from Walter (1998) and Kinzler, (1997), respectively.

Our results suggest that, even at low degrees of partial melting (i.e., <1%), the LREE composition of the diorite gabbro suite cannot be explained by non-modal melting (Shaw, 1970) of depleted mid-ocean ridge basalt or primitive mantle sources (Fig. 14a). Partial melting of spinel lherzolite sources produce magmas with Sm/Yb ratios similar to the source, whereas partial melting of a garnet lhzerolite with residual garnet produces melts with higher Sm/Yb ratios than the DMM-PM "mantle" array (Fig. 14b). The diorite-gabbro suite of this study possesses Sm/Yb ratios greater than even small degrees of partial melting of these potential mantle sources and is displaced from the mantle array (Fig. 14b). Thus, the diorite-gabbro suite requires a REE enriched source (e.g., a more differentiated source) and/or REE enrichment during magma-crust interaction. Furthermore, depleted Nb/Ta (18–5) and enriched Zr/Hf ratios (50–39) relative to chondritic values (Nb/Ta = 17.6; Zr/Hf = 36.3) suggest these rocks are not mantle-derived magmas (Green, 2006). Volcanic arcs are thought to possess depleted mantle sources that may be enriched in LILE and REE by a subduction component and/or interaction with the crust (Pearce, 1996b), whereas continental arcs are known to have sources that vary in composition from the upper mantle (i.e, fertile MORB mantle) to more enriched mantle (Pearce and Parkinson, 1993). Alternatively, REE enrichment within the diorite-gabbro suite may be due to melting a differentiated source in the lower crust. The exact source of the diorite-gabbro suite is unclear because of a lack of petrogenetic constraints on melting processes, however our REE modelling results are consistent with the trace element evidence (discussed in more detail below) that supports the involvement of crust-magma interaction.

5 Discussion

5.1 Archean granitoid petrogenesis

Here we show that previously considered Proterozoic granites are in fact Archean (ca. 2.74 Ga). Furthermore, inherited zircon ages from sample CL1020 provide evidence for >2.74 Ga crust beneath the Lupa Terrane. Other metamorphic belts surrounding the southern and eastern margins of the Tanzanian Craton (e.g., Mozambique and Usagaran) also contain Archean crust (Muhongo et al., 2001; Reddy et al., 2003; Sommer et al., 2003). These studies proposed that large portions of metamorphic belts enveloping the Tanzanian Craton represent re-worked Archean crust and are consistent with a growing number of deep seismic studies that demonstrate laterally extensive Archean lithosphere underlying many Proterozoic accretionary orogens (Snyder, 2002). Alternatively, Archean rocks may be unrelated to the Tanzanian Craton and may have been incorporated within these metamorphic belts during accretion (Muhongo et al., 2001).

The SW extent of the Tanzanian cratonic margin is a subject of debate (e.g., Coolen, 1980; Pinna et al., 2008). Manya (2011) proposed a possible location for the Tanzanian cratonic margin based on Sm-Nd isotopic evidence. However, a sample from Manya (2011) was taken from an outcrop in the Lupa Terrane and possessed an Archean Nd model age (i.e., 2688 Ma). That Archean sample is ca. 150 km away from the newly proposed Tanzanian cratonic margin and Manya (2011) interpreted the anomalous age as either a sliver of tectonically interleaved Archean material or re-melting of Archean crust. Archean foliated granites in the Lupa Terrane are older (ca. 2740 Ma) than Rb-Sr and K-Ar ages for the Tanzanian craton (2.4–2.6 Ga; Cahen et al., 1984) but are in good agreement with re-worked Archean rocks in the Usagaran (ca. 2700 Ma; Reddy et al., 2003) and Mozambique Belts [2740–2608 (Muhongo et al., 2001); 2970–2500 Ma (Sommer et al., 2003)] and recent U-Pb zircon SIMS ages for the Tanzanian Craton (>3.6–2.6 Ga; Kabete et al., 2012a, b).

U-Pb and Lu-Hf isotopic evidence provides petrogenetic evidence that constrains the geologic setting of the Archean granitoids. U-Pb zircon ages from CL098, CL109, and CL1020 record multiple zircon populations that have undergone non-zero Pb-loss, nevertheless interpreted crystallization ages are broadly within analytical uncertainty at ca. 2.74 Ga. The $^{176}Hf/^{177}Hf_{initial}$ ratios for interpreted magmatic zircon crystals from all three samples are also largely within analytical uncertainty (2σ) and suggests that all three foliated granitoid samples possess a homogeneous $^{176}Hf/^{177}Hf$ source. Calculated εHf values (-2.2–2.8) plot lower than the depleted mantle (Griffin et al., 2000) and the Neo-Mesoarchean mantle (Shirey et al., 2008) evolution curve (Fig. 11c). Juvenile melts (i.e., mantle melts) are expected to possess $^{176}Hf/^{177}Hf_{initial}$ compositions that overlap with the $^{176}Hf/^{177}Hf$ composition of the mantle source and our results imply that foliated granitoids are not juvenile mantle melts but likely formed from melting > 2.74 Ga crust (Fig. 11c). Melting was likely related to an Archean volcanic-arc that is consistent with the subduction signature suggested by the Archean granitoids trace element compositions (e.g., LREE enrichment; steeply dipping REE patterns; negative Nb and Ti anomalies; Figs. 13e, f).

Crustal residence ages (CR) can be estimated from the calculated $^{176}Hf/^{177}Hf_{initial}$ values and assuming a Lu-Hf composition of the mantle source (e.g., Shirey et al., 2008 and references therein). Our two-stage Lu-Hf model ages are subject to large uncertainties because of ^{176}Lu decay constant uncertainty, the poorly constrained Lu-Hf isotopic composition of the source, uncertainty regarding the $^{207}Pb/^{206}Pb$ crystallization age of the samples and uncertainties on individual Lu-Hf measurements (e.g., Davis et al., 2005). As a result, a range of model ages can be calculated from a single zircon crystal (e.g., Whitehouse and Kemp, 2010). The arithmetic average CR age for samples CL098, CL109, and CL1020 (not including inherited zircon crystals) is 3.1 Ga (± 0.9 Ga 2SD; n = 46). The significance of this age is unclear because of the limitations described above, however depleted mantle ages provide the first evidence for ≥ 3.1 Ga basement underlying the Lupa Terrane. The age of this basement is consistent with Nd model ages (2.8–3.1 Ga) from the Tanzanian Craton, Usagaran Belt, and the Mozambique Belt (Maboko, 1995; Maboko and Nakamura, 1996; Möller et al., 1998; Kabete et al., 2012a).

CL1020 includes inherited zircon crystals with $^{207}Pb/^{206}Pb$ ages ca. 100 Myr older than the interpreted crystallization age at ca. 2.74 Ga. The $^{176}Hf/^{177}Hf_{initial}$ values for suspected inherited zircon crystals are generally lower (arithmetic average = 0.281010 ± 0.000045 at 2SD, n =26) but possess significant overlap with zircon crystals that are thought to represent crystallization of CL1020 at ca. 2.74 Ga (arithmetic average = 0.281032 ± 0.000029 at 2SD, n = 16). Therefore, in addition to older $^{207}Pb/^{206}Pb$ ages the suspected inherited zircon crystals appear to have a different $^{176}Hf/^{177}Hf$ source than the magmatic zircon crystals. We propose that ca. >2.74 Ga zircon crystals represent an inherited zircon component that may have been sourced from several protoliths of different ages or a single protolith that crystallized at ca. 2.85 Ga and subsequently underwent non-zero Pb-loss to produce a range of $^{207}Pb/^{206}Pb$ ages (Friend and Kinny, 1995). We favour the latter interpretation because the

$^{177}Hf/^{176}Hf_{initial}$ ratios of inherited zircon crystals are largely within analytical uncertainty of each other and suggest a common $^{176}Hf/^{177}Hf_{initial}$ source.

Previous workers have suggested that Archean rocks within the Ubendian and Usagaran Belts were tectonically interleaved during accretion (Muhongo et al., 2001; Manya, 2011). This hypothesis seems unlikely in the Lupa Terrane where magmatic contacts are clearly observed between the Archean and Paleoproterozoic granitoids (e.g., Fig. 4c). Seismic tomography models provide evidence for re-worked Archean crust and upper lithosphere extending SW from the Tanzanian Craton to the Bangweulu Block (see Fig. 2 of Begg et al., 2009). If correct, significant portions of the Ubendian Belt may represent re-worked Archean crust. Our U-Pb and Lu-Hf support this hypothesis and we propose that the Tanzanian cratonic margin is located at least 150 km SW from its currently accepted position (Manya, 2011; Figs. 1). Our proposed model implies that Archean granitoids are present between Lake Rukwa and currently known exposures of the Tanzanian Craton near the town of Rungwa, but may be difficult to identify in the field as a result of reworking and/or the intrusion of voluminous Paleoproterozoic granitoids.

5.2 Paleoproterozoic Granitoid and Diorite-Gabbro Petrogenesis

Ratios of highly incompatible elements have been shown to remain unchanged during large degrees of partial melting or crystal fractionation (e.g., Pearce and Peate, 1995). Thus incompatible elements can be used as tracers for magmatic processes. One important element for tracing subduction zone processes is Nb, which is preferentially retained in the down-going slab within mineral phases (e.g., rutile; Pearce and Peate, 1995). Nb depletions, such as those exhibited by Lupa Terrane intrusive phases, are therefore characteristic of melts generated in volcanic arcs (Figs. 13d). The diorite-gabbro suite also displays other trace element compositions that are typical of volcanic rocks erupting at modern day volcanic-arcs. LREE enrichment (Hildreth and Moorbath, 1988), low TiO_2 contents (i.e., <2.0 wt. %; Pearce and Cann, 1973), large Ba/Ta and Ba/Nb ratios (i.e., >450, and >28, respectively; Gill, 1981), low Y/Cr ratios (Pearce, 1982), high Th/Nb and Ce/Nb ratios (Saunders et al., 1988) all suggest the diorite-gabbro suite are typical of calc-alkaline subduction-related (i.e., volcanic-arc) magmas (Fig. 15). The diorite-gabbro suite also plots in the island-arc field of La-Sm-Th-Yb-Nb log-transformed discrimination diagrams (Agrawal et al., 2008; Figs. 15e, f). Paleoproterozoic granitoids also possess trace element characteristics typical of volcanic arcs (e.g., Nb and Ti depletions, high Hf/Ta ratios range from 2–9; Pearce et al., 1984; Harris et al., 1986). Furthermore, the concave-up pattern of the granodiorite samples (CL0975; CL0911; CL0921; CL0958) are typical of volcanic-arc granites in which MREE strongly partition into hydrous phases, such as amphibole, during crystallization (Pearce, 1996b; Fig. 13).

Volcanic-arc melts, oceanic or continental, typically originate as a result of partial melting of depleted asthenosphere. Subduction processes (e.g., metasomatism in mantle wedge) and crust-magma interaction (e.g., Melting-Assimilation-Segregation-Homogenization; Hildreth and Moorbath, 1988) can then modify the trace element composition of melt products (e.g., LILE and LREE enrichment). Therefore, distinguishing source characteristics from crust-magma interaction is difficult using trace element compositions alone (e.g., Davidson, 2005). Paleoproterozoic granitoids and the diorite-gabbro suite are observed cross cutting Archean granitoids. Field observations and inherited zircon crystals (e.g., CL1019) suggest that Paleoproterozoic magmatic phases likely interacted with this evolved Archean crust (e.g., La/Yb_{cn} = 28.8–64.6) during emplacement. Crust-magma interaction is typical of continental arcs and can explain the enriched LREE signature of Lupa Terrane lithologies (REE modelling; Fig. 14). Large variations in LILE/HFSE ratios (e.g., Ba/La) between broadly contemporaneous and spatially overlapping magmatic phases are more readily explained by varying degrees of crustal-magma interaction and magmatic processes rather than variability within melt sources (Hildreth and Moorbath, 1998). We therefore propose that trace element compositions of Paleoproterozoic magmatic phases are typical of continental arcs that exhibit evidence for crust-magma interaction, and that low Ti-Nb-Ta values argue against an intraplate tectonic setting.

5.3 Geochronologic Constraints on Deformation and Metamorphism

The U-Pb geochronologic data from the current study constrains the absolute timing of deformation events within the Lupa Terrane. At least three, temporally distinct, deformation events (D1, D2, D3) are recognized in the field. The first deformation event (D1) is only developed within the Archean granitoids. Undulating chlorite-rich bands separated by bands of K-feldspar, plagioclase, and quartz give Archean granitoids a banded appearance. This tectonic fabric varies in intensity from outcrop to outcrop but is consistently present across the field area. Archean foliated granitoids are cross cut by non-foliated Paleoproterozoic granites, granodiorites, diorites, and gabbros. Our U-Pb data broadly constrains the timing of D1 to between 2.72 and 1.96 Ga. Brittle-ductile mylonititc shear zones (D2) crosscut all of the dated magmatic phases. This deformation event is economically important as these structures are the primary host for Au mineralization (Lawley et al., in press). Our U-Pb data constrains the timing of D2 to <1.89 Ga and is consistent with Re-Os dating of syn-deformational pyrite at ca. 1.88 Ga (Lawley et al., in press). Greenschist facies metamorphism is characteristic of the Au bearing shear zones and overprints all of the dated igneous phases. The timing of greenschist facies metamorphism is therefore <1.89 Ga but likely related to D2 at ca. 1.88 Ga. Gold- and pyrite-bearing quartz veins (D2) are locally crosscut by discrete brittle faults (D3). The timing of D3 is not constrained, however the brittle nature of the faults is in contrast to the ductile nature of deformation during D1 and D2 and suggests that D3 deformation may have occurred at significantly shallower depths within the crust (Lawley et al., in press). The proposed temporally distinct deformation events are only those that are readily distinguished in the field and it is expected that Paleoproterozoic structures have been reactivated during tectonism that has continued to the present day (Theunissen et al., 1996).

The U-Pb lower intercept ages reported as part of this study potentially provide evidence for younger metamorphic overprints that broadly overlap with orogenic cycles recorded in the other Ubendian Terranes (Boniface et al., 2012; Boniface and Schenk, 2012). For example, an imprecise U-Pb lower intercept age for sample CL0911 (1126 ± 150 Ma) provides evidence for a Mesoproterozoic Pb-loss event that is broadly equivalent to the Kibaran and/or Irumide orogenic cycles (de Waele et al., 2009), whereas imprecise U-Pb lower intercept ages for samples CL109 (512 ± 140 Ma), CL1021 (524 ± 140 Ma) and CL1022 (469 ± 89 Ma), are broadly contemporaneous with the Pan African Orogeny (Hanson, 2003). New U-Pb geochronology thus provides evidence for three orogenic cycles that hitherto are unreported for the Lupa Terrane, but additional geochronology is required before determine the significance and distribution of these younger metamorphic overprints.

5.4 Geodynamic Model

Paleoproterozoic magmatic rocks in the Lupa Terrane possess trace element compositions that are typical of continental volcanic-arcs. Based on the geologic, geochronologic, and geochemical evidence presented above we propose that the Lupa Terrane was a continental-arc during the Paleoproterozoic. In our model, the Lupa Terrane represents the continental margin (i.e., the Tanzanian cratonic margin) to which allochthonous terranes (i.e., other Ubendian Terranes) were accreted. The 1.96–1.88 Ga magmatic events in the Lupa Terrane are younger than the 2.1–2.0 Ga Ubendian tectonic phase but are in good agreement with the second Ubendian Tectonic phase at 1.9–1.8 Ga. Current geochronologic constraints suggest that the Katuma-Ufipa-Lupa Terranes possess the oldest ages (i.e., >1900 Ma) and are separated by the disparately younger Ubende-Mbozi Terrane (i.e., <1900 Ma). Our U-Pb crystallization ages (1960–1880 Ma) overlap with ages reported from each of the lithotectonic terranes; however no ages reported in this study are comparable to the ca. 1860 Ma eclogites in the Ubende Terrane (Boniface et al., 2012). The Katuma Terrane (1977–1900 Ma; Boniface, 2009) lies along strike of the northwest trending Lupa Terrane and possess a similar magmatic history that suggests both Terranes may have shared a similar tectono-magmatic evolution.

Recent ages constraining the temporal evolution of the Ubendian Belt are incompatible with the existing tectonic model (Fig. 1b; Daly, 1988). For example, any geodynamic model must explain the juxtaposition of greenschist facies metamorphism in the Lupa Terrane and contemporaneous amphibolite-granulite facies metamorphism in the other Ubendian Terranes. The existing model of wrench-dominated tectonics would require several hundred kilometres of lateral displacement to explain this juxtaposition (Fig. 1b; Daly, 1988). Alternatively, subduction-related thrusting could have brought high-grade metamorphic rocks in adjacent Ubendian Terranes to the same structural level as the contemporaneous greenschist facies rocks comprising the Lupa Terrane. Our model would imply that sub-horizontal lineations on the terrane-bounding shear zones may be related to strike-slip reactivation of terrane sutures rather than Paleoproterozoic lateral accretion. The timing of this juxtaposition is unclear as Mesoproterozoic, Neoproterozoic and Tertiary Rifting all likely contributed to the current configuration of Ubendian Terranes (Boniface, 2009; Boniface et al., 2012; Boniface and Schenk, 2012). The exact geodynamic evolution of the Ubendian Belt remains enigmatic and requires additional constraints. Our results are however consistent with a protracted accretion history during the 1.9–1.8 Ubendian tectonic phase (Boniface et al., 2009).

6 Summary and Conclusions

The magmatic history of the Lupa Terrane began in the Archean (ca. 2.74 Ga) with the intrusion of evolved, calc-alkaline, and arc-type granites. Inherited U-Pb zircon ages and Lu-Hf zircon isotopic evidence imply that these granites are the products of partial melting and incorporation of substantially older crust (ca. 3.1 Ga). Archean granitoids were structurally deformed to produce a weakly developed schistosity (D1; 2.74–1.96 Ga) and were then intruded by Paleoproterozoic (1.96–1.88 Ga) calc-alkaline granitoids (syenogranites, monzogranites, and granodiorites) and dioritic-gabbroic intrusions. Paleoproterozoic igneous lithologies are crosscut by Au-bearing and greenschist facies shear zones (D2) that host the orogenic gold deposits of the Lupa Terrane. Based on the U-Pb, Lu-Hf, trace element and field evidence presented above we propose:

- At least a 150km SW extension of the Tanzanian cratonic margin to the Rukwa escarpment. Our results are consistent with seismic tomography studies that provide evidence for Archean upper lithosphere extending SW from the Tanzanian Craton to the Bangweulu Block (Begg et al., 2009).
- That Paleoproterozoic magmatic activity possesses trace element characteristics that are analogous to modern-day continental arcs.
- That the Lupa Terrane acted as the continental margin onto which the other Ubendian Terranes were accreted during the Paleoproterozoic. Inherited zircon crystals, trace elements and REE modelling suggest the diorite-gabbro suite underwent magma-crust interaction, which is consistent with a continental arc setting.
- That Paleoproterozoic eclogites with MORB-like chemistry (Boniface et al., 2012) imply subduction and thrusting were important accretion processes in contrast to the wrench-dominated tectonics proposed by Daly (1988). Thrusting could also explain the juxtaposition

of contemporaneous greenschist facies metamorphism in the Lupa with amphibolite-granulite facies metamorphism characteristic of the other Ubendian Terranes.

Acknowledgements

Funding and support was provided by a Durham Doctoral Fellowship at Durham University and student research grant from the Society of Economic Geologists to CJML. Helio Resource Corp. kindly provided funding, and access to drill core/exploration licenses for sampling. This work benefitted from discussion with Nelson Boniface and Bruce Kjarsgaard. Two anonymous reviewers also greatly improved the manuscript.

Electronic Supplement: Analytical Methods

Zircon Mineral Separation

Zircon crystals were separated from their host rock by crushing ~5 kg of rock in a jaw crusher and pulverizing in a disc mill before passing the sample through a 355 µm sieve. Samples were then placed on a Rogers shaking table and the heavy fraction dried (at 60ºC) before passing through a Frantz isodynamic magnetic separator. The non-magnetic fractions of each sample were then density separated using methylene iodide before handpicking, under ethanol, of the most crack- and inclusion-free grains.

U-Pb Zircon ID-TIMS

All the analyzed zircon crystals have undergone the "chemical abrasion" (thermal annealing and subsequent leaching) pre-treatment technique (Mattinson, 2005) for the effective elimination of Pb-loss. This involved placing zircon crystals in a muffle furnace at 900 ± 20°C for ~60 hours in quartz beakers before being transferred to 3ml Hex Savillex beakers, placed in a Parr vessel, and leached in a ~5:1 mix of 29M HF + 30% HNO3 for 12 hours at ~180°C. The acid solution was removed, and fractions were rinsed in ultrapure H2O, fluxed on a hotplate at ~80°C for an hour in 6 M HCl, ultrasonically cleaned for an hour, and then placed back on the hotplate for an additional 30 min. The HCl solution was removed and the fractions (single zircon crystals or fragments) were selected, photographed (in transmitted light) and again rinsed (in ultrapure acetone) prior to being transferred to 300 µl Teflon FEP microcapsules and spiked with a mixed ^{233}U–^{235}U–^{205}Pb tracer. Zircon was dissolved in ~120 µl of 29 M HF with a trace amount of 30% HNO3 with microcapsules placed in Parr vessels at ~220°C for 48 hours, dried to fluorides, and then converted to chlorides at ~180°C overnight. U and Pb for all minerals were separated using standard HCl-based anion-exchange chromatographic procedures.

Isotope ratios were measured at the NERC Isotope Geosciences Laboratory (NIGL), UK, using a Thermo-Electron Triton Thermal Ionisation Mass-Spectrometer (TIMS). Pb and U were loaded together on a single Re filament in a silica-gel/phosphoric acid mixture. Pb was measured by peak-hopping on a single SEM detector. U isotopic measurements were made in static Faraday mode. Age calculations and uncertainty estimation (including U/Th disequilibrium) was based upon the algorithms of Schmitz and Schoene (Schmitz and Schoene, 2007).

U-Pb Zircon LA-MC-ICP-MS

Laser Ablation Multi-Collector Inductively Coupled Plasma Mass Spectrometry (LA-MC-ICP-MS) was conducted at the NERC Isotope Geoscience Laboratory (NIGL). Zircon mineral separates were mounted in epoxy, polished, and imaged using cathodoluminesence (CL) on a scanning electron microscope (SEM) at the British Geological Survey (with the exception of CL098 which was prepared at the School of Natural Sciences, Trinity College Dublin). CL imaging provided textural information that assisted zircon targeting. Zircon crystals were ablated using a New Wave Research UP193SS Nd:YAG laser ablation system and an in-house built low-volume rapid washout ablation cell. Ablated material was transported from the ablation cell using a continuous flow of He gas to a Nu Plasma MC-ICP-MS equipped with a multi-ion-counting array. ^{207}Pb, ^{206}Pb and ^{204}Pb+Hg isotopes were measured on ion counters whereas U and Tl isotopes and ^{202}Hg were measured using faraday cups. Data were collected using the Nu Instruments time resolved analysis software. Prior to analysis, the MC-ICP-MS was tuned and gains were measured using a Tl-^{235}U solution co-aspirated using a Nu Instruments DSN-100 desolvating nebuliser. At the start of each run an instrument zero was measured for 30s and was followed by three 30s ablations of three reference materials. The internationally recognized 91500 reference zircon (Weidenbeck et al., 1995) was used as the primary reference material, whereas Plešovice (Sláma et al., 2008) and GJ-1 (Jackson et al., 2004) were used as validation materials. All three matrix matched materials were used to monitor instrumental drift and 91500 was used to correct for instrumental drift. The nine standard ablations were followed by ca. twelve 30s sample ablations. Once data stability had been established replicates were dropped to one to two for each reference materials. All ablations used a 25–30 μm static spot at 5 Hz, and a fluence of 2.7 J/cm^2. During each analysis the co-aspirated Tl-^{235}U solution was used to correct for instrumental mass bias and plasma induced elemental fractionation. The interference of ^{204}Hg on ^{204}Pb was monitored and corrected for by simultaneously measuring ^{202}Hg and assuming a ^{204}Hg/^{202}Hg = 0.229887. U-Pb data were processed using an in-house spread sheet at NIGL.

All presented ^{206}Pb/^{238}U dates (ID-TIMS and LA-ICP-MS) are calculated using the ^{238}U and ^{235}U decay constants of Jaffey et al. (Jaffey et al., 1971). The consensus value of ^{238}U/^{235}U = 137.818 ± 0.045 (Hiess et al., 2012) was used in the data reduction calculations. Using this more accurate value with its associated uncertainty estimate has the effect of lowering ^{207}Pb/^{206}Pb dates at c. 2 Ga by 0.8 ± 0.6 Myr, compared to ^{207}Pb/^{206}Pb dates calculated using the consensus value of ^{238}U/^{235}U = 137.88. For U–Pb dates of this age the ^{206}Pb/^{238}U dates are the most precise and robust. In contrast, the ^{207}Pb-based dates (^{207}Pb/^{235}U and ^{206}Pb/^{207}Pb) are considerably less precise and hence are only used to assess concordance of the U–Pb (zircon) systematics.

References

Agrawal, S., Guevara, M., and Verma, S., 2008. Tectonic discrimination of basic and ultrabasic volcanic rocks through log-transformed ratios of immobile trace elements. International Geology Review 50, 1057–1079.

Begg, G.C., Griffin, W.L., Natapov, L.M., O'Reilly, S.Y., Grand, S.P., O'Neill, C.J., Hronsky, J.M.A., Poudjom Djomani, Y., Swain, C.J., Deen, T., and Bowden, P., 2009. The lithospheric architecture of Africa: seismic tomography, mantle petrology, and tectonic evolution. Geosphere 5, 23–50.

Boniface, N., 2009. Eburnian, Kibaran, and Pan-African metamorphic events in the Ubendian Belt of Tanzania; petrology, zircon and monazite geochronology. Unpublished PhD thesis, Kiel University, Germany, 110 p.

Boniface, N., Schenk, V., and Appel, P., 2012. Paleoproterozoic eclogites of MORB-type chemistry and three Proterozoic orogenic cycles in the Ubendian Belt (Tanzania): evidence from monazite and zircon geochronology, and geochemistry. Precambrian Research 192–195, 16–33.

Boniface, N., and Schenk, V., 2012. Neoproterozoic eclogites in the Paleoproterozoic Ubendian Belt of Tanzania: evidence for a Pan-African suture between the Bangweulu Block and the Tanzania Craton. Precambrian Research 208–211, 72–89.

Boven, A., Theunissen, K., Skylarov, E., Klerkx, J., Melnikov, A., Mruma, A., and Punzalan, L., 1999. Timing of exhumation of a high-pressure mafic granulite Terrane of the Paleoproterozoic Ubende Belt (west Tanzania). Precambrian Research 93, 119–137.

Brock, P.W.G., 1963. The Mbozi syenite-gabbro complex. Unpublished PhD Thesis, University of Leeds, UK, 261 p.

Cahen, L., Snelling, N.J., Delhal, J., and Vail, J., 1984. The geochronology and evolution of Africa, Clarendon Press, Oxford.

Chauvel, C., and Blichert-Toft, J., 2001. A hafnium isotope and trace element perspective on melting of the depleted mantle. Earth and Planetary Science Letters 190, 137–151.

Collins, A.S., Reddy, S.M., Buchan, C., and Mruma, A., 2004. Temporal constraints on Palaeoproterozoic eclogite formation and exhumation (Usagaran, Orogen, Tanzania). Earth and Planetary Science Letters 224, 175–192.

Coolen, J.J.M.M.M., 1980. Chemical petrology of the Furua Granulite Complex, southern Tanzania: Unpublished PhD thesis, 13Vrije University, Amsterdam, GUA pap. Geol., Ser. 1, 258 p.

Daly, M.C., 1988. Crustal shear zones in central Africa; a kinematic approach to Proterozoic tectonics. Episodes 11, 5–11.

Dampare, S.B., Shibata, T., Asiedu, D.K., Osae, S., and Banoeng-Yakubo, B., 2008. Geochemistry of Paleoproterozoic metavolcanic rocks from the southern Ashanti volcanic belt, Ghana: Petrogenetic and tectonic setting implications: Precambrian Research 162, 403–423.

Davidson, J.P., Hora, J.M., Garrison, J.M., and Dungan, M.A., 2005. Crustal forensics in arc magmas. Journal of Volcanology and Geothermal Research 140, 157–170.

Davis, D.W., Amelin, Y., Nowell, G.M., and Parrish, R.R., 2005. Hf isotopes in zircon from the western Superior Province, Canada: Implications for Archean crustal development and evolution of the depleted mantle reservoir. Precambrian Research 140, 132–156.

de Waele, B., Fitzsimons, I.C.W., Wingate, M.T.D., Timbo, F., Mapani, B., and Belousova, E.A., 2009. The geochronological framework of the Irumide Belt: A prolonged crustal history along the margin of the Bangweulu Craton. American Journal of Science 309, 132–187.

Dodson, M.H., Cavanagh, B.J., Thatcher, E.C., and Aftalion, M., 1975. Age limits for the Ubendian metamorphic episode in northern Malawi. Geological Magazine 112, 403–410.

Friend, C.R.L., and Kinny, R.D., 1995. New evidence for protolith ages of Lewisian granulites, northwest Scotland. Geology 23, 1027–1030.

Floyd, P.A., and Winchester, J.A., 1975. Magma type and tectonic setting discrimination using immobile elements. Earth and Planetary Science Letters 27, 211–218.

Gabert, G. and Wendt, I. 1974. Datierung von granitischen Gesteinen im Dodoman- und Usagaran-System und in der Ndembera-Serie (Tanzania). Geologische Jahrbuch, B 11, 3–55.

Gallagher, D.R., 1939. Preliminary account of the geology of a portion of Lupa goldfield. Economic Geology 34, 306–323.

Gerdes, A., and Zeh, 2009. Zircon formation versus zircon alteration – new insights from the combined U-Pb and Lu-Hf in-situ LA-ICP-MS analyses, and consequences for the interpretation of Archean zircon from the Central Zone of the Limpopo Belt. Chemical Geology 261, 230–243.

Gill, J.B., 1981. Orogenic Andesites and Plate Tectonics, Springer-Verlag, Berlin.

Grant, J.A., 2005. Isocon analysis; a brief review of the method and applications. Physics and Chemistry of the Earth, Parts A/B/C, 30, 997–1004.

Grantham, D.R., 1931. Lupa river goldfield. Mining Magazine 45, 265–276.

Grantham, D.R., 1932. Lupa goldfield. Bulletin of the Geological Survey of Tanganyika 3, 34 p.

Grantham, D.R., 1933. The eastern extension of Lupa goldfield. Geological Survey of Tanganyika, short paper 11, 9 p.

Green, N.L., 2006. Influence of slab thermal structure on basalt source regions and melting conditions: REE and HFSE constraints from the Garibaldi volcanic Belt, northern Cascadia subduction system. Lithos 87, 23–49.

Griffin, W.L., Pearson, N.J., Belousova, E., Jackson, S.E., van Achterbergh, E., O'Reilly, S.Y., Shee, S.R., 2000. The Hf isotope composition of cratonic mantle: LAM-MC-ICPMS analysis of zircon megacrysts in Kimberlites. Geochimica et Cosmochimica Acta 64, 133–147.

Hanson, R.E., 2003, Proterozoic geochronology and tectonic evolution of southern Africa, in: Yoshida, M., Windley, B.F., and Dasgupta, S., (Eds.), Proterozoic East Gondwana: Supercontinent Assembly and Breakup, Geological Society, London, Special Publications 206, pp. 427–463.

Harris, J.F., 1961. Summary of geology of Tanganyika. Geological Survey of Tanganyika Memoir 1, 64–67.

Harris, N.B.W., Pearce, J.A., and Tindle, A.G., 1986. Geochemical characteristics of collision-zone magmatism, in: Coward, M.P., and Ries, A.C., (Eds.), Collision Tectonics, Geological Society Special Publications 19, pp. 51–81.

Hiess, J., Condon, D. J., McLean, N., and Noble, S. R., 2012. $^{238}U/^{235}U$ Systematics in Terrestrial Uranium-Bearing Minerals. Science 335 (no. 6076), 1610-1614.

Hildreth, W., and Moorbath, S., 1988. Crustal contributions to arc magmatism in the Andes of central Chile. Contributions to Mineralogy and Petrology 98, 455–489.

Jackson, S.E., Pearson, N.J., Griffin, W.L., and Belousova, E.A., 2004. The application of laser ablation-inductively coupled plasma-mass spectrometry to in situ U-Pb zircon geochronology. Chemical Geology 211, 47–69.

Jaffey, A. H., Flynn, K. F., Glendenin, L. E., Bentley, W. C., and Essling, A. M., 1971. Precision measurement of half-lives and specific of ^{235}U and ^{238}U. Physics Reviews C4, 1889-1906.

Kabete, J.M., McNaughton, N.J., Groves, D.I., and Mruma, A.H., 2012a. Reconnaissance SHRIMP U-Pb zircon geochronology of the Tanzania Craton: Evidence for Neoarchean granitoid-greenstone belts in the Central Tanzania Region and the Southern East African Orogen. Precambrian Research 216–219, 232–266.

Kabete, J.M., Gorves, D.I., McNaughton, N.J., and Mruma, A.H., 2012b, A new tectonic and temporal framework for the Tanzanian Shield: Implications for gold metallogeny and undiscovered endowment. Ore Geology Reviews 48, 88–124.

Kemp, A.I.S., Foster, G.L., Scherstén, A., Whitehouse, M.J., Darling, J., and Storey, C., 2009. Concurrent Pb-Hf isotope analysis of zircon by laser ablation multi-collector ICP-MS, with implications for the crustal evolution of Greenland and the Himalayas. Chemical Geology 261, 244–260.

Kilembe, E.A., and Rosendahl, B.R., 1992. Structure and stratigraphy of the Rukwa rift. Tectonophysics 209, 143–158.

Kimambo, R.H.N., 1984. Mining and mineral prospects in Tanzania, Eastern Africa Publications Ltd., Arusha.

Kinzler, R.J., 1997. Melting of mantle peridotite at pressures approaching the spinel to garnet transition: applications to mid-ocean ridge basalt petrogenesis. Journal of Geophysical Research 102, 853–874.

Kröner, A., Muhongo, S., Hegner, E., and Wingate, M.T.D., 2003. Single-zircon geochronology and Nd isotopic systemtics of Proterozoic high-grade rocks from the Mozambique belt of southern Tanzania (Masasi area): implications for Gondwana assembly. Journal of the Geological Society 160, 745–757.

Lawley, C.J.M., 2012. Geochronology and structure of the Lupa goldfield, Tanzania. Unpublished PhD thesis, Durham University, Durham, UK, 219 p.

Lawley, C.J.M., Selby, D., and Imber, J., in press, Re-Os Molybdenite, pyrite and chalcopyrite geochronology, Lupa Goldfield, SW Tanzania: Tracing metallogenic time scales at mid-crustal shear zones hosting orogenic Au deposits: Economic Geology.

Lawley, C.J.M., Imber, J., and Selby, D., in press, Structural controls on orogenic Au-mineralization along a non-Andersonian fault/shear zone system: Lupa goldfield, SW Tanzania: Economic Geology.

LeMaitre, R.W., Streckeisen, A., Zanettin, B., Le Bas, M.J., Bonin, B., and Bateman, P., 2002. Igneous rocks: a classification and glossary of terms; recommendations of the International Union of Geological Sciences Subcommission on the systematics of igneous rocks, Cambridge University Press, Cambridge.

Lenoir, J.L., Liégeois, J.P., Theunissen, K., and Klerkx, J., 1994. The Palaeoproterozoic Ubendian shear Belt in Tanzania: geochronology and structure. Journal of African Earth Sciences 19, 169–184.

Ludwig, K.A. 2008. User's Manual for Isoplot 3.6, A Geochronological Toolkit for Microsoft Excel. Berkeley Geochronology Center Special Publication No. 4, 77 p.

Maboko, M.A.H., 1995. Neodymium isotopic constraints on the protolith ages of rocks involved in Pan-African tectonism in the Mozambique Belt of Tanzania. Journal of the Geological Society 152, 911–916.

Maboko, M.A.H., and Nakamura, E., 1996. Nd and Sr isotopic mapping of the Archaean-Proterozoic boundary in southeastern Tanzania using granites as probes for crustal growth. Precambrian Research 77, 105–115.

Manya, S., 2011. Nd-isotope mapping of the Archean-Proterozoic boundary in southwestern Tanzania: implication for the size of the Archean Tanzanian Craton. Gondwana Research 20, 325–334.

Manya, S., 2012. SHRIMP zircon U-Pb dating of the mafic and felsic intrusive rocks of the Saza area in the Lupa goldfields, southwestern Tanzania: Implications for gold mineralization: Natural Science 4, 724–730.

Marobhe, I., 1989. Interpretation of aerogeophysical anomalies of southwestern Tanzania. Geological Survey of Finland Bulletin 350, 72 p.

Mattinson, J.M., 2005. Zircon U-Pb chemical abrasion ("CA-TIMS") method: combined annealing and multi-step partial dissolution analysis for improved precision and accuracy of zircon ages. Chemical Geology 220, 47–66.

McConnell, R.B., 1950. Outline of the geology of Ufipa and Ubende. Geological Survey of Tanganyika Bulletin 19, 62 p.

McKenzie, D., and O'Nions, R.K., 1991. Partial melt distribution from inversion of rare earth element concentrations. Journal of Petrology 32, 1021–1091.

Meschede, M., 1986. A method of discriminating between different types of mid-ocean ridge basalts and continental tholeiites with the Nb-Zr-Y diagram. Chemical Geology 56, 207–218.

Mnali, S.R., 1999. Palaeoproterozoic felsic magmatism and associated gold-quartz vein mineralization in the western part of the Lupa goldfield, south-western Tanzania. Unpublished PhD thesis, University of Dar es Salaam, Tanzania 198 p.

Mnali, S.R., 2002. Tectonic setting of gabbroic rocks in the western part of the Lupa gold field, south-west Tanzania. Tanzanian Journal of Science 28, 99–113.

Möller, A., Appel, P., Mezger, K., and Schenk, V., 1995. Evidence for a 2 Ga subduction zone: eclogites in the Usagaran Belt of Tanzania. Geology 23, 1067–1070.

Möller, A., Mezger, K., and Schenk, V., 1998. Crustal age domains and the evolution of the continental crust in the Mozambique Belt of Tanzania: combined Sm-Nd, Rb-Sr, and Pb-Pb isotopic evidence. Journal of Petrology 39, 749–783.

Muhongo, S., Tuisku, P., Mnali, S., Temu, E., Appel, P., and Stendal, H., 2001. High-pressure granulite-facies metagabbros in the Ubendian Belt of SW Tanzania: preliminary petrography and P-T estimates. Journal of African Earth Sciences 34, 279–285.

Nowell, G.M., and Parrish, R.R., 2001, Simultaneous acquisition of isotope compositions and parent/daughter ratios by non-isotope dilution-mode plasma ionisation multi-collector mass spectrometry (PIMMS), in: Holland, G. and Tanner, S.D., (Eds.), Plasma Source Mass Spectrometry: The New Millenium. Royal Chemical Society, Special Publication 267, pp. 298–310.

Patchett, P.J., and Tatsumoto, M., 1980. Halfnium isotope variations in oceanic basalts. Geophysical Research Letters 7, 1077–1080.

Pearce, J.A., and Cann, J.R., 1973. Tectonic setting of basic volcanic rocks determined using trace element analysis. Earth and Planetary Science Letters 19, 290–300.

Pearce, J.A., 1982. Trace element characteristics of lavas from destructive plate boundaries, in: Thorpe, R.S., (Ed.), Andesites. Wiley, New York, pp. 525–548.

—, 1983. Role of the subcontinental lithosphere in magma genesis at active continental margins, in: Hawkesworth, C.J., and Norry, M.J., (Eds.), Continental Basalts and Mantle Xenoliths. Cheshire, UK, Shiva Press Ltd., pp. 230–249.

Pearce, J.A., Harris, N.B.W., and Tindle, A.G., 1984. Trace element discrimination diagrams for the tectonic interpretation of granitic rocks. Journal of Petrology 25, 956–983.

Pearce, J.A., and Parkinson, I.J., 1993. Trace element models for mantle melting: application to volcanic arc petrogenesis, in: Prichard, H.M., Alabaster, T., Harris, N.B.W., and Neary, C.R., (Eds.), Magmatic Processes and Plate Tectonics. Geological Society Special Publication 76, pp. 373–403.

Pearce, J.A., and Peate, D.W., 1995. Tectonic implications of the composition of volcanic arc magmas. Annual Review of Earth and Planetary Sciences 23, 251–285.

Pearce, J.A., 1996a. A user's guide to basalt discrimination diagrams, in: Wyman, D.A., (Ed.), Trace Element Geochemistry of Volcanic Rocks: Applications for Massive Sulphide Exploration. Geological Association of Canada, Short Course Notes 12, pp. 79–113.

—, 1996b. Sources and settings of granitic rocks. Episodes 19, 120–125.

Pietranik A.B., Hawkesworth C.J., Storey C.D., Kemp A.I.S., Sircombe K.N., Whitehouse M.J., and Bleeker W., 2008. Episodic mafic crust formation from 4.5 to 2.8 Ga: New evidence from detrital zircons, Slave craton, Canada. Geology 36, 875–878.

Pinna, P., Muhongo, S., Mcharo, A., Le Goff, E., Deschamps, Y., Ralay, F., Milesi, J.P., 2008. Geology and mineral map of Tanzania. Geological Survey of Tanzania, Dodoma.

Priem, H.N.A., Boelrijk, N.A.I.M., Hebeda, E.H., Verdurmen, E.A.T., Verschure, R.H., Oen, I.S., and Westra, L., 1979. Isotopic age determinations on granitic and gneissic rocks from the Ubendian-Usagaran system in southern Tanzania. Precambrian Research 9, 227–239.

Reddy, S.M., Collins, A.S., and Mruma, A., 2003. Complex high-strain deformation in the Usagaran Orogen, Tanzania: structural setting of Palaeoproterozoic eclogites. Tectonophysics 375, 01–123.

Reddy, S.M., and Evans, D.A.D., 2009. Palaoproterozoic supercontinents and global evolution: correlations from core to atmosphere, in: Reddy, S.M., Mazumder, R., Evans, R., and Collins, D.A.D., (Eds.), Palaeoproterozoic Supercontinents and Global Evolution. Geological Society Special Publications 232, pp. 1–26.

Ring, U., 1993. Aspects of the kinematic history and mechanisms of superposition of the Proterozoic mobile Belts of eastern Central Africa (northern Malawi and southern Tanzania). Precambrian Research 62, 207–226.

Ring, U., Kröner, A., and Toulkeridis, T., 1997. Palaeoproterozoic granulite-facies metamorphism and granitoid intrusions in the Ubendian-Usagaran Orogen of northern Malawai, east-central Africa. Precambrian Research 85, 27–51.

Sango, P.M., 1988. Structural and lithological controls of gold mineralization in the Lupa goldfield, Tanzania, in: Ho, S.E., and Groves, D.I., (Eds.), Recent Advances in Understanding Precambrian Gold Deposits. Geology Department and University Extension, The University of Western Australia, Publication No. 12, pp. 99–109.

Saunders, A.D., Norry, M.J., and Tarney, J., 1988. Origin of MORB and chemically-depleted mantle reservoirsL: trace element constraints. Journal of Petrology (Special Lithosphere Issue), 415–445.

Schandelmeier, H., 1983. The geochronology of post-Ubendian granitoids and dolerites from the Mambwe area, northern province, Zambia. Report Institute Geological Sciences 83, 40–46.

Shaw, D.M., 1970. Trace element fractionation during anatexsis. Geochimica Cosmochimica Acta 34, 237–243.

Schmitz, M.D., and Schoene, B., 2007. Derivation of isotope ratios, errors, and error correlations for U-Pb geochronology using ^{205}Pb-^{235}U(^{233}U)-spiked isotope dilution thermal ionization mass spectrometric data. Geochemistry, Geophysics, Geosystems 8, 20 p.

Shervais, J.W., 1982. Ti-V plots and the petrogenesis of modern ophiolitic lavas. Earth and Planetary Science Letters 59, 101–118.

Shirey, S.B., Kamber, B.S., Whitehouse, M.J., Mueller, P.A., and Basu, A.R., 2008. A review of the isotopic and trace element evidence for mantle and crustal processes in the Hadean and Archaean: implications for the onset of plate tectonic subduction, in: Condie, K.C., and Pease, V.L., (Eds.), When did Plate Tectonics Start on Earth?, Geological Society of America, Memoir 440, pp. 1–29.

Simpson, R., 2012. NI 43-101 mineral resource estimate update for the Saza-Makongolosi Gold Project, Tanzania. Unpublished SRK consulting report, 217 p.

Sláma, J., Košler, J., Condon, D.J., Crowley, J.L., Gerdes, A., Hanchar, J.M., Horstwood, M.S.A., Morris, G.A., Nasdala, L., Norberg, N., Schaltegger, U., Schoene, B., Tubrett, M.N., Whitehouse, M.J., 2008. Plesovice zircon — a new natural reference material for U-Pb and Hf isotopic microanalysis. Chemical Geology 249, 1–35.

Smirnov, V., Pentel'kov, V., Tolochko, V., Trifan, M., and Zhukov, S., 1973. Geology and minerals of the central part of the western rift. Report on Geological Mapping, Mineral and Resource Division, Dodoma, Tanzania, 333 p.

Sommer, H., Kröner, A., Hauzenberger, C., Muhongo, S., and Wingate, M.T.D., 2003. Metamorphic petrology and zircon geochronology of high-grade rocks from the central Mozambique Belt of

Tanzania: crustal recycling of Archean and Paleoproterozoic material during the Pan-African orogeny. Journal of Metamorphic Geology 21, 915–934.

Sommer, H., Kröner, A., Muhongo, S., and Hauzenberger, C., 2005. Ages for post-Usagaran granitoid and rhyolitic rocks, Tanzania. South African Journal of Geology 108, 247–256.

Sun, S.S., and McDonough, W.F., 1989. Chemical and isotopic systematics of ocean basalts; implications for mantle composition and processes, in: Saunders, A.D., Norry, M.J., (Eds.), Magmatism in Ocean Basins. Geological Society of London Special Publication 42, pp. 313–345.

Sutton, J., Watson, J., and James, T.C., 1954. A study of the metamorphic rocks of Karema and Kungwe bay, western Tanganyika. Bulletin of the Geological Survey of Tanganyika 22, 70 p.

Snyder, D.B., 2002. Lithospheric growth at margins of cratons. Tectonophysics 355, 7–22.

Teale, E.O., Eades, N.W., Harkin, D.A., Harpum, J.R., and Horne, R.G., 1935. Brief explanation of the geology of Irambo area, quarter degree sheet 245, Geological Survey of Tanganyika, Dodoma.

Theunissen, K., Lenoir, J. L., Liégeois, J-P., Delvaux, D., and Mruma, A., 1992. Empreinte pan-africaine majeure dans la chaine ubendienne de Tanzanie sud-occidentale: geochronologie U-Pb sur zircon et contexte structural. Comptes Rendus de l'Académie des Sciences 314, 1355–1362.

Theunissen, K., Klerkx, J., Melnikov, A., and Mruma, A., 1996. Mechanisms of inheritance of rift faulting in the western branch of the east African Rift, Tanzania. Tectonics 15, 776–790.

Van Straaten, V.P., 1984. Gold Mineralization in Tanzania – a review, in: Foster, R.P., (Eds.), Gold '82: the Geology, Geochemistry and Genesis of Gold Deposits. A.A. Balkema, Rotterdam, pp. 673–685.

Vervoort, J.D. and Blichert-Toft, J., 1999. Evolution of the depleted mantle: Hf isotope evidence from juvenile rocks through time. Geochimica et Cosmochimica Acta 63, 533–556.

Walter, M.J., 1998. Melting of garnet peridotite and the origin of komatiite and depleted lithosphere. Journal of Petrology 39, 29–60.

Wendt, I., Besang, C., Harre, W., Kreuzer, H., Lenz, H. and Muller, P. 1972. Age determinations of granitic intrusions and metamorphic events in the early Precambrian of Tanzania. Proceedings of 24th International Geological Congress, Montreal, Canada, pp 295–314 (section 1).

Whitehouse, M.J., and Kemp, A.I.S., 2010. On the difficulty of assigning crustal residence, magmatic protolith and metamorphic ages to Lewisian granulites: constraints from combined in situ U-Pb and Lu-Hf isotopes, in: Law, R.D., Butler, R.W.H., Holdsworth, R.E., Krabbendam, M., and Strachan, R.A., (Eds.), Continental Tectonics and Mountain Building; the Legacy of Peach and Horne. Geological Society Special Publications 335, pp. 81–101.

Winchester, J.A., and Floyd, P.A., 1977. Geochemical discrimination of different magma series and their differentiation products using immobile elements. Chemical Geology 20, 325–343.

Wiedenbeck, M., Allé, P., Corfu, F., Griffin, W.L., Meier, M., Oberli, F., Von Quadt, A., Roddick, J.C., and Spiegel, W., 1995. Three natural zircon standards for the U-Th-Pb, Lu-Hf, trace element and REE analysis. Geostandards and Geoanalytical Research 19, 1–23.

Wood, D.A., 1980. The application of a Th-Hf-Ta diagram to problems of tectonomagmatic classification and to establishing the nature of crustal contamination of basaltic lavas of the British Tertiary volcanic province. Earth and Planetary Sciences Letters 50, 11–30.

Zhoa, G., Cawood, P.A., Wilde, S.A., and Sun, M., 2002. Review of global 2.1–1.8 Ga orogens: implications for a pre-Rodinia supercontinent. Earth Science Reviews 59, 125–162.

Figure Captions

Figure 1

(a) Regional geology map of SW Tanzania showing Ubendian Terranes (modified from Daly, 1988); (b) existing tectonic model for Paleoproterozoic accretion of Ubendian Terranes (Daly, 1988).

Figure 2

Regional geologic map showing Ubendian Terranes and previously reported geochronology sample locations (modified from Smirnov et al., 1973).

Figure 3

Local geology map showing the location of geochronology and lithogeochemistry samples. Inferred lithologic contacts are based on a series of river traverses by the first author and are integrated with unpublished aeromagnetic and radiometric surveys, acquired from Helio Resource Corp. Shear zone locations are based, in part, on mapping and correspond to negative magnetic anomalies, whereas dikes are buried and interpreted from linear magnetic highs. Contour lines are based on an unpublished digital elevation model by Helio Resource Corp. and are shown at 5 m intervals.

Figure 4

(a) Folded banding in Archean granite in sharp contact with massive gabbroic dike; (b) well developed banding in foliated granite; (c) foliated Archean granitoid (CL098) cross cut by massive granodiorite dike (CL0911); (d) weathered surface of Ilunga Syenogranite that gives surface expposures a grey appearance. When fresh, modally dominant pink K feldspar crystals are visible. Narrow aplitic dike observed crosscutting the Ilunga Syenogranite; (e) Ilunga Syenogranite in drill core from Porcupine ore body; (f) gold- and pyrite-bearing quartz vein cross cutting Ilunga Syenogranite; (g) mafic enclave suggesting the Ilunga Syenogranite is pre-dated by mafic intrusions; (h) porphyritic monzogranite showing characteristic K feldspar phenocrysts; (i) Saza Granodiorite cross cut by aplite dike. The pitted weathered profile is typical of Saza Granodiorite outcrops; (j) Saza Granodiorite in drill core (CL1030).

Figure 5

(a) Typical example of the diorite-gabbro suite in core; (b) finer grained example of diorite-gabbro suite with more felsic enclaves; (c) plagioclase-amphibole intergrowths in diorite; (d) core photo of an example of the undifferentiated diorite-gabbro-granodiorite unit (Fig. 3) showing variable grain-size and modal mineralogy at hand sample scale; (e) complex and poly-phase mafic enclave hosted by granodiorite. Note ductile flow evidence around the enclave; (f) late fine-grained and alkaline dike (CL0956) cross cutting foliated Archean granitoid.

Figure 6

(a) Transmitted light photomicrograph of primary Fe-Mg minerals in foliated Archean granite that have been replaced by chlorite, titanite, epidote, and opaques; (b) transmitted light photomicrograph of rare relict amphibole in a granodiorite dike that has been overprinted by chlorite and epidote; (c) transmitted light photomicrograph of diorite dike showing characteristic mineral assemblage of amphibole, plagioclase, quartz, titanite, and epidote; (d) crossed nicols transmitted light photomicrograph of recrystallized quartz grain boundaries in foliated Archean granitoid. Quartz crystals also locally possess undulatory extinction and subgrain development; (e) crossed nicols transmitted light photomicrograph of sericitized plagioclase; (f) crossed nicols transmitted light photomicrograph of micrographic texture in Ilunga Syenogranite. Locally, Ilunga Syenogranite samples possess gradational contacts with aplite dikes and are characterized by abundant feldspar intergrowth textures.

Figure 7

Concordia plots for CL0911, CL0972, and CL0975, respectively. See text for discussion.

Figure 8

(a) Cathodoluminesence image of zircon F1 from CL109 showing ablation spots and concordant $^{207}Pb/^{206}Pb$ ages; (b) cathodoluminesence image of zircon H1 from CL1019 showing ablation spots and concordant $^{207}Pb/^{206}Pb$ ages; (c) cathodoluminesence image of zircon J8 from CL1020 showing U-Pb and Lu-HF ablation spots and concordant $^{207}Pb/^{206}Pb$ ages; (e) cathodoluminesence image of zircon B1 from CL1022 showing ablation spots and concordant $^{207}Pb/^{206}Pb$ ages.

Figure 9

(a, b) Concordia plots of all Archean LA-MC-ICP-MS zircon analyses and concordant (>95% concordance) analyses, respectively. See text for discussion.

Figure 10

(a, heb) Concordia plots of all Proterozoic LA-MC-ICP-MS zircon analyses and concordant (>95% concordance) analyses, respectively. See text for discussion.

Figure 11

(a) Measured $^{176}Hf/^{177}Hf$ ratios from CL098, CL109, and CL1020. Overlying individual analyses are the probability distributions for each sample. Samples CL098 and CL1020 possess approximately normal $^{176}Hf/^{177}Hf$ ratios distributions, whereas CL109 possesses a weakly bi-modal distribution. (b) Calculated $^{176}Hf/^{177}Hf_{initial}$ ratios for sample CL098, CL109, and CL1020 plotted against each analyses corresponding $^{207}Pb/^{206}Pb$ age. The CHUR evolution line and typical 2σ uncertainty for an individual analysis are also shown. (c) Calculated εHf for samples CL098, CL109, and CL1020 plotted against the corresponding $^{207}Pb/^{206}Pb$ age for each analysis. DM (MORB source depleted mantle, Griffin et al., 2000), Slave Craton mantle (Pietranik et al., 2008), and Neo-Mesoarchean mantle (Shirey et al.,

2008) are also plotted. The typical 2σ uncertainty on individual $^{207}Pb/^{206}Pb$ ages and εHf values are also shown.

Figure 12

Trace element rock classification diagram (modified from Pearce, 1996a). See text for discussion.

Figure 13

(a) REE plot of felsic phases normalized to CL chondrite (Sun and McDonough, 1989); (b) trace element plot of felsic phases normalized to primitive mantle (Sun and McDonough, 1989); (c) REE plot of intermediate-mafic phases normalized to CL chondrite (Sun and McDonough, 1989); (d) trace element plot of intermediate-mafic phases normalized to primitive mantle (Sun and McDonough, 1989); (e) REE plot of foliated Archean granitoids plotted with Tanzania Craton REE sample range from Manya (2011). REE are normalized to CI chondrite (Sun and McDonough, 1989). (f) trace element plot of foliated Archean granitoids plotted with Tanzania Craton REE sample range from Manya (2011). Trace elements are normalized to primitive mantle (Sun and McDonough, 1989). Sample symbols are the same as Fig. 12.

Figure 14

(a) La vs. La/Sm plot of diorite-gabbro suite. (b) Sm vs. Sm/Yb plot of diorite gabbro suite. Melting curves are from the non-modal batch melting equations of Shaw (1970). The modelling used spinel lherzolite (with mode = olivine$_{53}$ + orthopyroxene$_{27}$ + clinopyroxene$_{17}$ + spinel$_{3}$; melt mode = olivine$_{6}$ + orthopyroxene$_{28}$ + clinopyroxene$_{67}$ + spinel$_{11}$; Kinzler, 1997) and garnet lherzolite (with mode = olivine$_{60}$ + orthopyroxene$_{20}$ + clinopyroxene$_{10}$ + garnet$_{10}$; melt mode = olivine$_{3}$ + orthopyroxene$_{16}$ + clinopyroxene$_{88}$ + garnet$_{9}$; Walter, 1998) sources with depleted mantle (DMM; McKenzie and O'Nions, 1991) and primitive mantle (PM; Sun and McDonough, 1989) compositions. Mineral/matrix partition coefficients are from McKenzie and O'Nions (1991). N-MORB and E-MORB compositions were taken from Sun and McDonough (1989). The solid line represents the mantle array and is defined using the DMM and PM compositions. Lithology sample symbols are the same as Fig. 12.

Figure 15

(a) Basaltoid tectonic discrimination diagram modified from Shervais (1982). VAB = volcanic arc basalt, MORB = mid-ocean ridge basalt, BAB = back-arc basin basalt, OIB = ocean island basalt, CAB = continental arc basalt; (b) basaltoid tectonic discrimination diagram modified from Wood (1980). N-MORB = normal-mid ocean ridge basalt; (c) basaltoid tectonic discrimination diagram modified from Meschede (1986). WPT = within-plate tholeitic basalt, WPA = within-plate alkalic basalt, P-type MORB = primitive mid-ocean ridge basalt, N-type MORB = normal-type mid-ocean ridge basalt; (d) basaltoid tectonic discrimination diagram modified from Pearce (1983). S = subduction zone enrichment trend, C = crustal contamination trend, F = fractional crystallization trend (F = 0.5); (e) log-transformed basaltoid discrimination diagram modified from Agrawal et al. (2008). $DF1=0.3518\ Log(La/Th)+0.6013\ Log(Sm/Th)-1.3450\ Log(Yb/Th)+2.1056\ Log(Nb/Th)-5.4763$; and $DF2 = -0.3050\ Log(La/Th) - 1.1801\ Log(Sm/Th) + 1.6189\ Log(Yb/Th) + 1.2260\ Log(Nb/Th) - 0.9944$. MORB = mid-ocean ridge basalts, IAB = island arc basalt, CRB = continental rift basalt, OIB = ocean island basalt; (f) log-transformed basaltoid discrimination diagrams modified from Agrawal et al. (2008). $DF1 = 0.5533\ Log(La/Th) + 0.2173\ Log(Sm/Th) - 0.0969\ Log(Yb/Th) + 2.0454\ Log(Nb/Th) - 5.6305$ and $DF2 = -2.4498\ Log(La/Th) + 4.8562\ Log(Sm/Th) - 2.1240\ Log(Yb/Th) - 0.1567\ Log(Nb/Th) + 0.94$. IAB = island arc basalt, OIB = ocean island basalt, CRB = continental rift basalt. Lithology symbols are the same as Fig. 12.

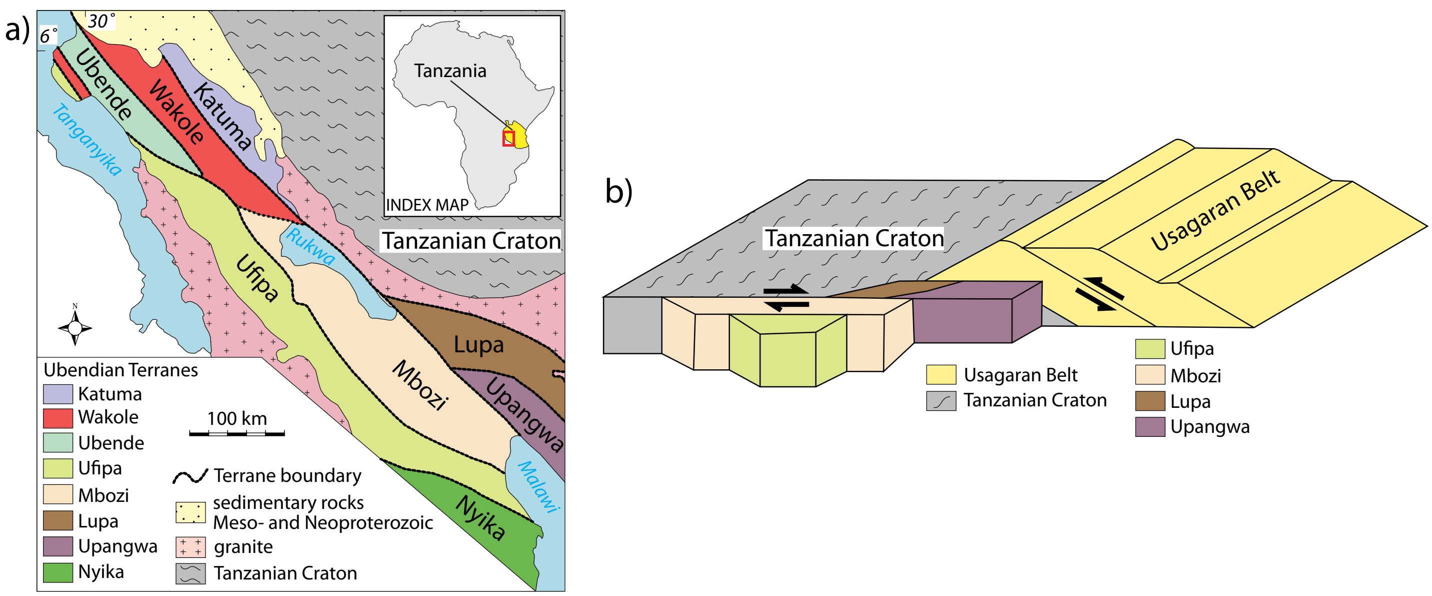
a)
6°
30°
Ubende
Wakole
Katuma
Tanganyika
Tanzania
INDEX MAP
Tanzanian Craton
Rukwa
Ufipa
Lupa
Mbozi
Upangwa
Malawi
Nyika
N
Ubendian Terranes
Katuma
Wakole
Ubende
Ufipa
Mbozi
Lupa
Upangwa
Nyika
100 km
Terrane boundary
sedimentary rocks
Meso- and Neoproterozoic
granite
Tanzanian Craton
b)
Tanzanian Craton
Usagaran Belt
Usagaran Belt
Tanzanian Craton
Ufipa
Mbozi
Lupa
Upangwa

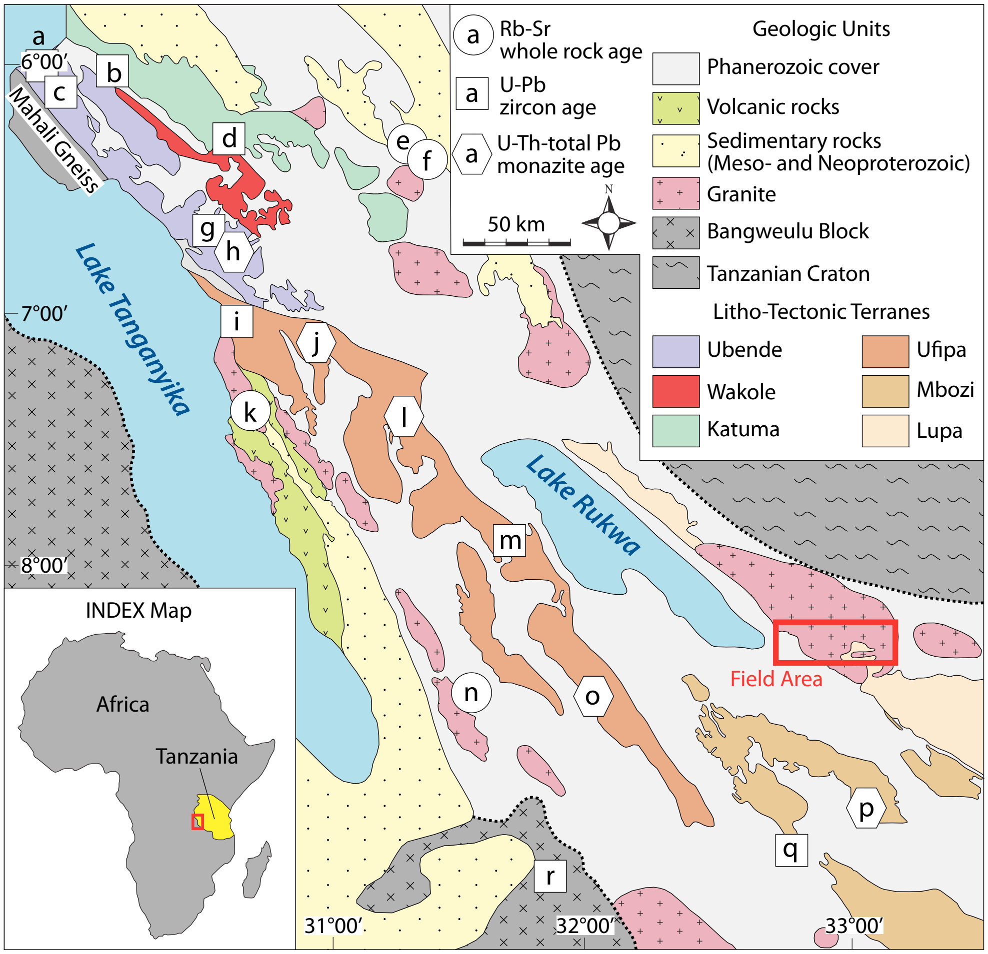

a 1854 ± 26 Ma (eclogite)[1]
b 1977 ± 40 Ma (mafic granulite)[1]
c 1817 ± 26 Ma (metapelite)[1]
1093 ± 10 Ma (metapelite)[1]
d 1900 ± 14 Ma (metapelite)[1]
e 1847 ± 37 Ma (granite)[2]
f 1902 ± 73 Ma (gneiss)[2]
g 1866 ± 14 Ma (eclogite)[1]
h 1831 ± 11 Ma (metapelite)[1]
1175 ± 10 Ma (metapelite)[1]
601 ± 7 Ma (metapelite)[1]
i 1864 ± 32 Ma (granite)[2]
j 1868 ± 55 Ma (metapelite)[1]
578 ± 63 Ma (metapelite)[1]
k 1725 ± 48 Ma (granite)[2]
l 566 ± 8 Ma (metapelite)[1]
m 1901 ± 37 Ma (metapelite)[1]
n 1723 ± 41 Ma (granite)[2]
o 1919 ± 12 Ma (metapelite)[1]
p 1814 ± 7 Ma (metapelite)[1]
q 743 ± 30 Ma (syenite)[3]
r 1838 ± 86 Ma (granite)[4]
s 1930 ± 30 Ma (Nyika granite; off map)[5]

[1]Boniface (2009); [2]Lenoir et al. (1994); [3]Brock (1963); [4]Schandelmeirer (1983); [5]Dodson et al. (1975)

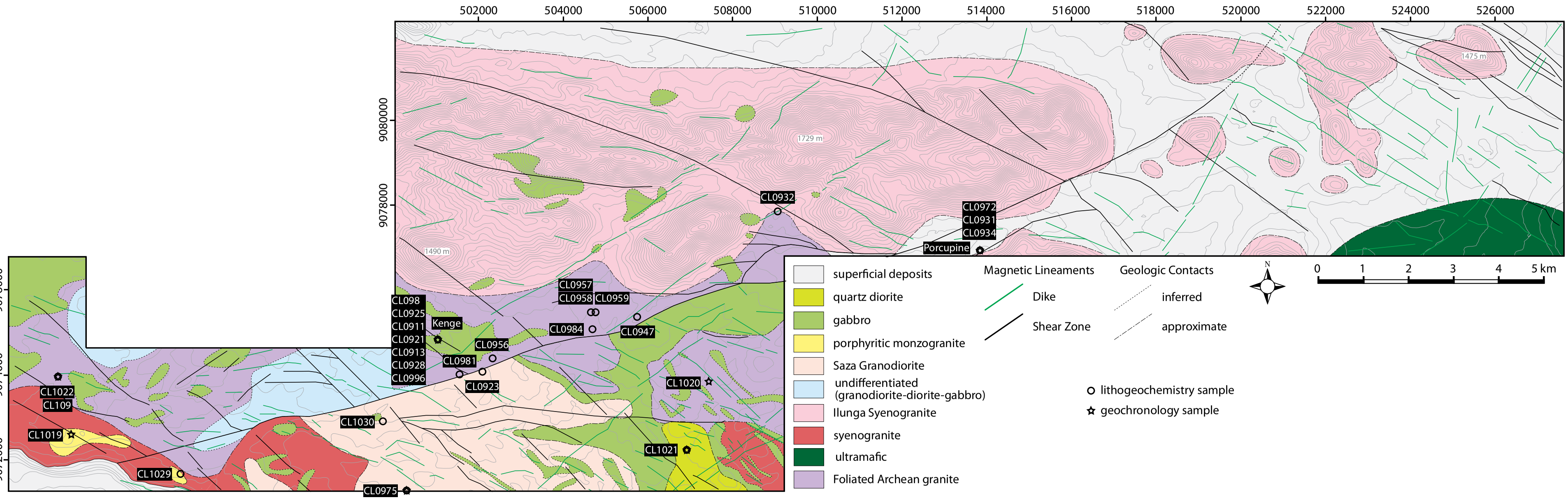
502000
504000
506000
508000
510000
512000
514000
516000
518000
520000
522000
524000
526000
9080000
9078000
9076000
9074000
9072000
1729 m
1490 m
1475 m
CL0932
CL0972
CL0931
CL0934
Porcupine
CL098
CL0925
CL0911
CL0921
CL0913
CL0928
CL0996
Kenge
CL0956
CL0981
CL0923
CL0957
CL0958
CL0959
CL0984
CL0947
CL1020
CL1021
CL1030
CL0975
CL1022
CL109
CL1019
CL1029
superficial deposits
quartz diorite
gabbro
porphyritic monzogranite
Saza Granodiorite
undifferentiated
(granodiorite-diorite-gabbro)
Ilunga Syenogranite
syenogranite
ultramafic
Foliated Archean granite
Magnetic Lineaments
Dike
Shear Zone
Geologic Contacts
inferred
approximate
lithogeochemistry sample
geochronology sample
N
0
1
2
3
4
5 km

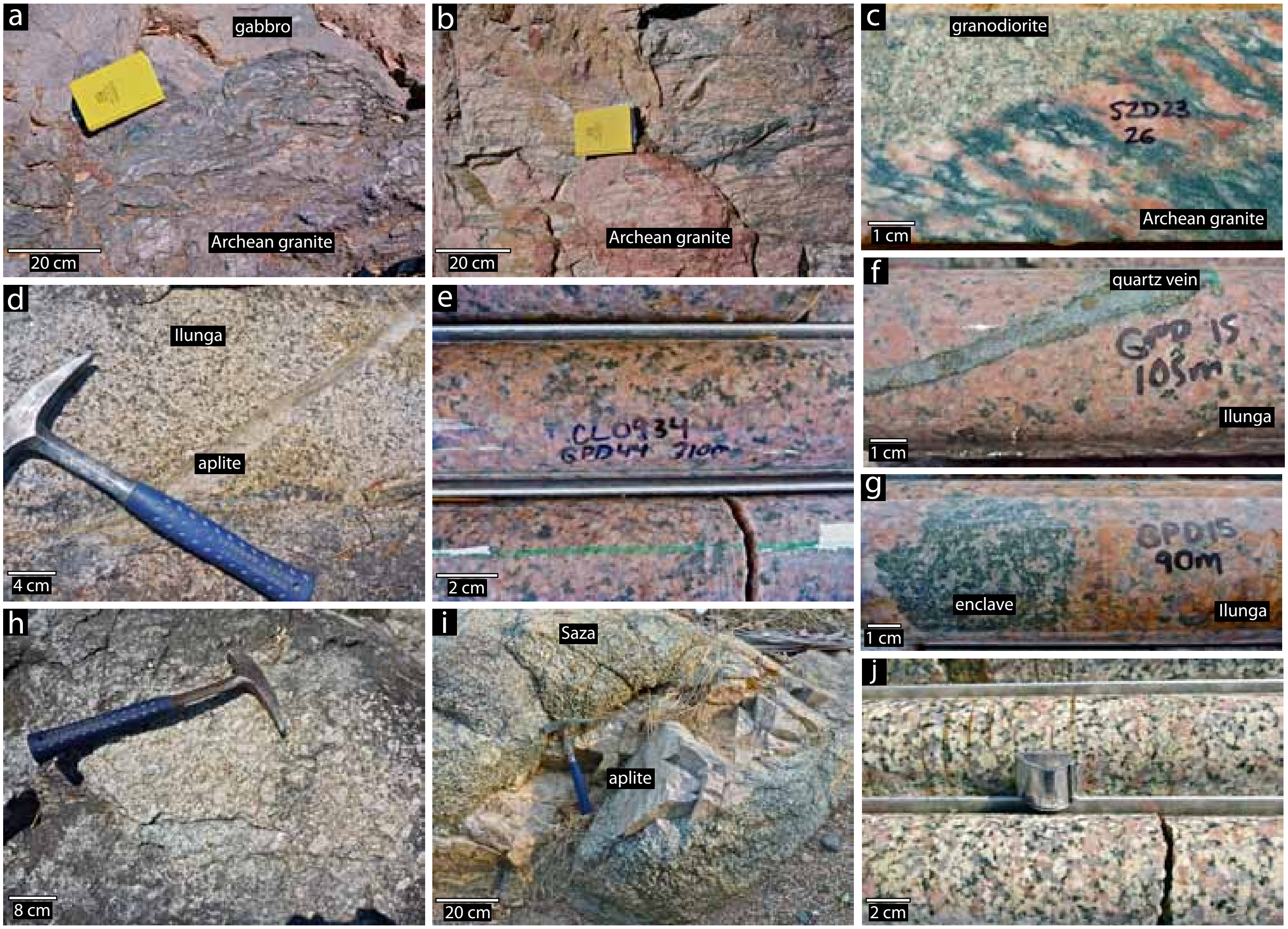
a
gabbro
Archean granite
20 cm
b
Archean granite
20 cm
c
granodiorite
SZD23
26
Archean granite
1 cm
d
Ilunga
aplite
4 cm
e
CL0934
GPD44
2 cm
f
quartz vein
GPD 15
105m
Ilunga
1 cm
g
GPD15
90m
enclave
Ilunga
1 cm
h
8 cm
i
Saza
aplite
20 cm
j
2 cm

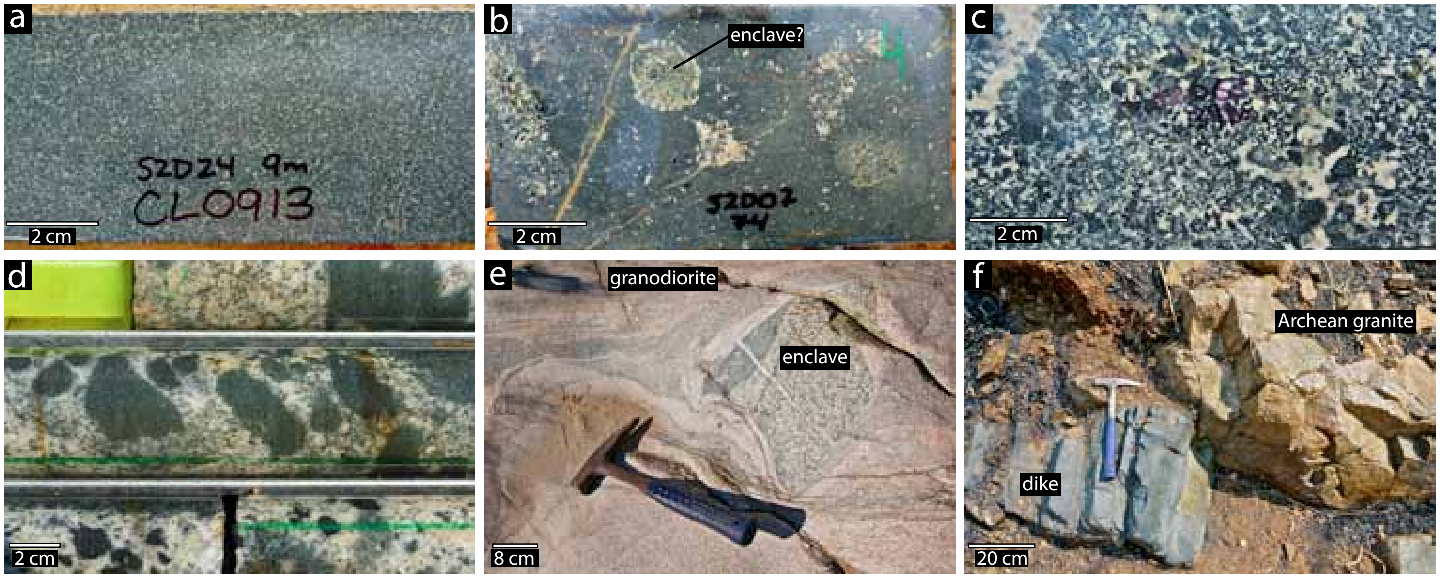
a
52D24 9m
CL0913
2 cm
b
enclave?
52D07
2 cm
c
2 cm
d
2 cm
e
granodiorite
enclave
8 cm
f
Archean granite
dike
20 cm

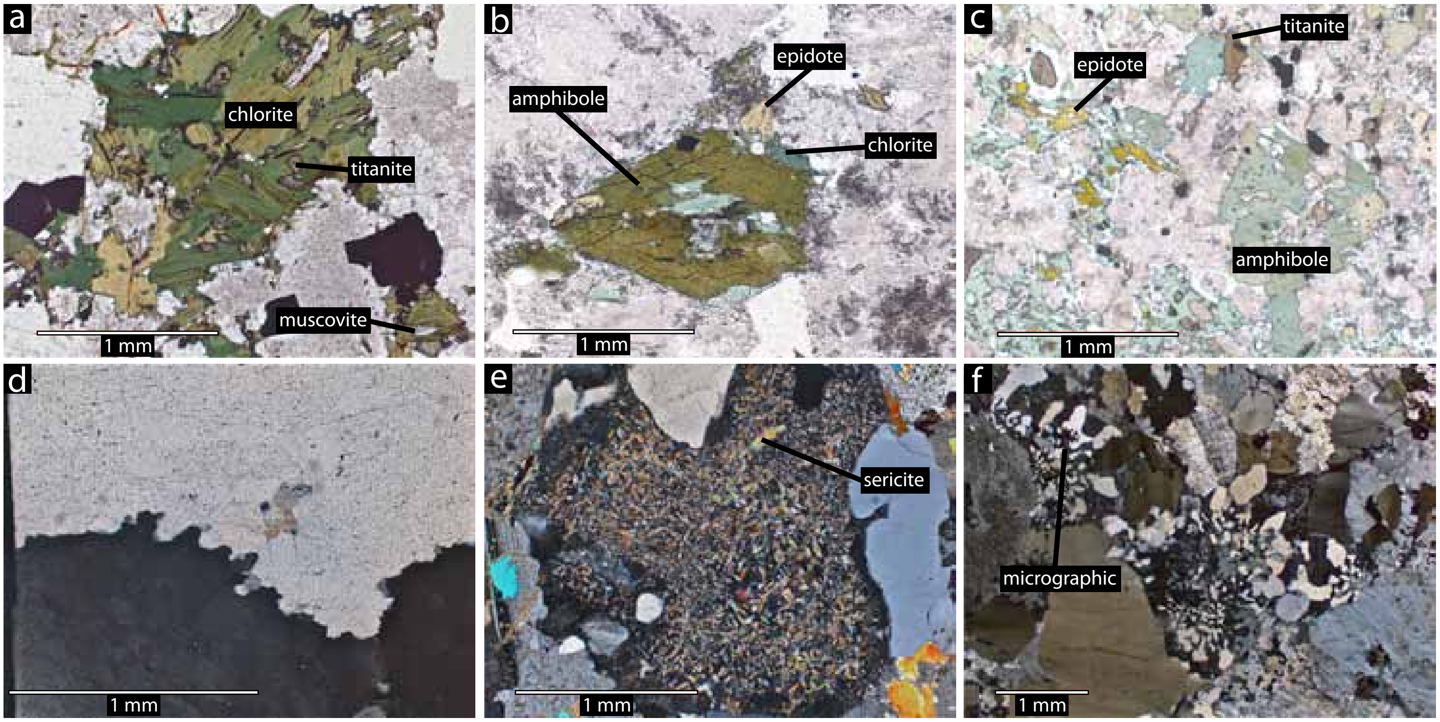
a
chlorite
titanite
muscovite
1 mm
b
epidote
amphibole
chlorite
1 mm
c
titanite
epidote
amphibole
1 mm
d
1 mm
e
sericite
1 mm
f
micrographic
1 mm

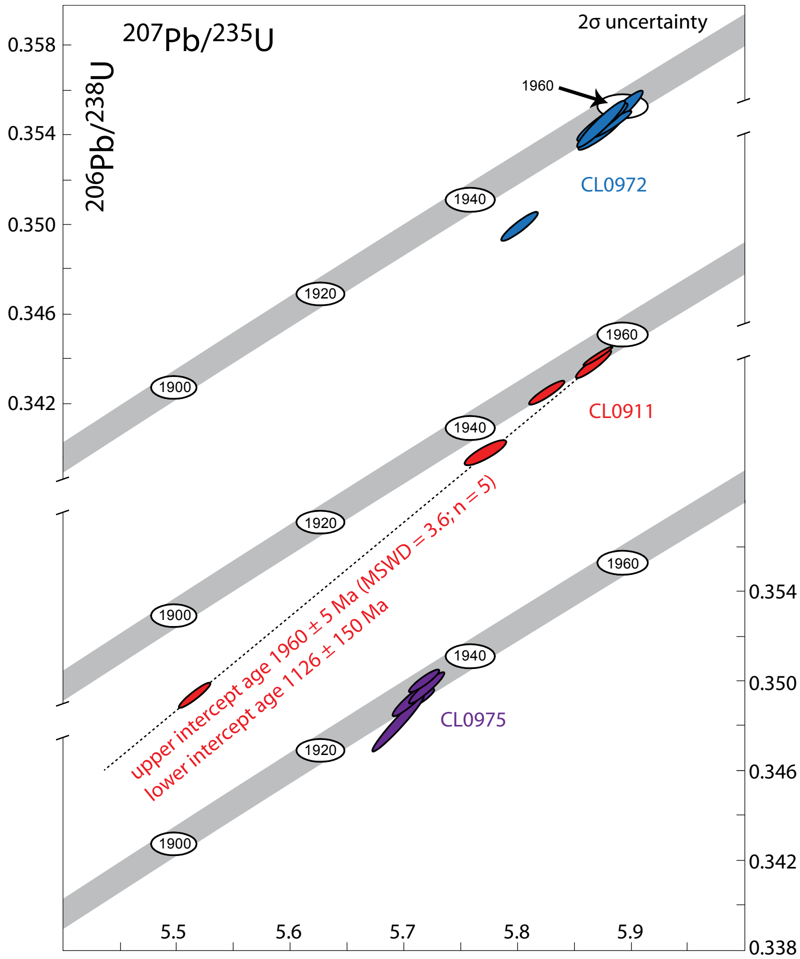

$^{207}Pb/^{235}U$
$^{206}Pb/^{238}U$
2σ uncertainty
0.358
0.354
0.350
0.346
0.342
0.338
5.5
5.6
5.7
5.8
5.9
1900
1920
1940
1960
CL0972
CL0911
CL0975
upper intercept age 1960 ± 5 Ma (MSWD = 3.6; n = 5)
lower intercept age 1126 ± 150 Ma

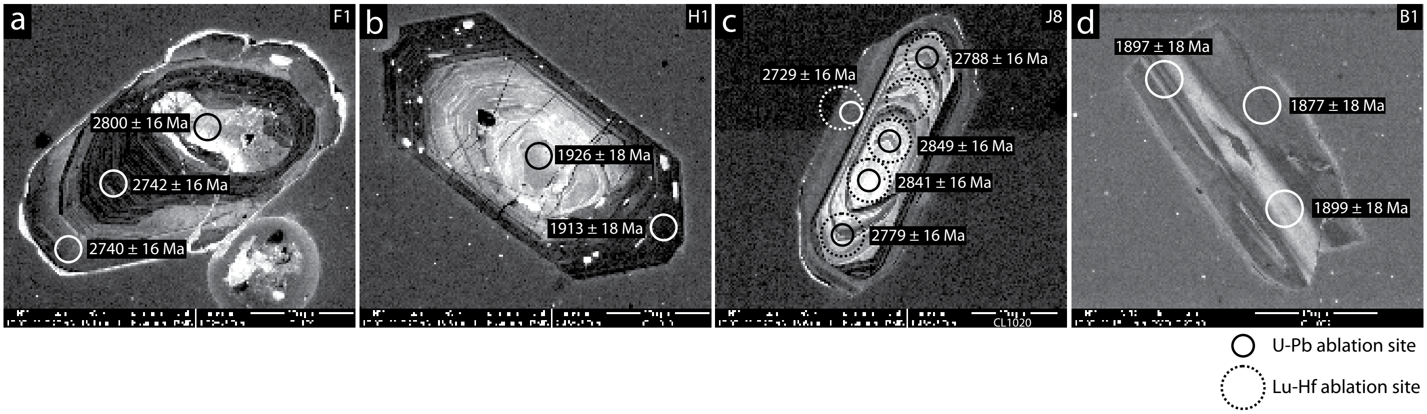

a
F1
2800 ± 16 Ma
2742 ± 16 Ma
2740 ± 16 Ma
b
H1
1926 ± 18 Ma
1913 ± 18 Ma
c
J8
2729 ± 16 Ma
2788 ± 16 Ma
2849 ± 16 Ma
2841 ± 16 Ma
2779 ± 16 Ma
CL1020
d
B1
1897 ± 18 Ma
1877 ± 18 Ma
1899 ± 18 Ma
U-Pb ablation site
Lu-Hf ablation site

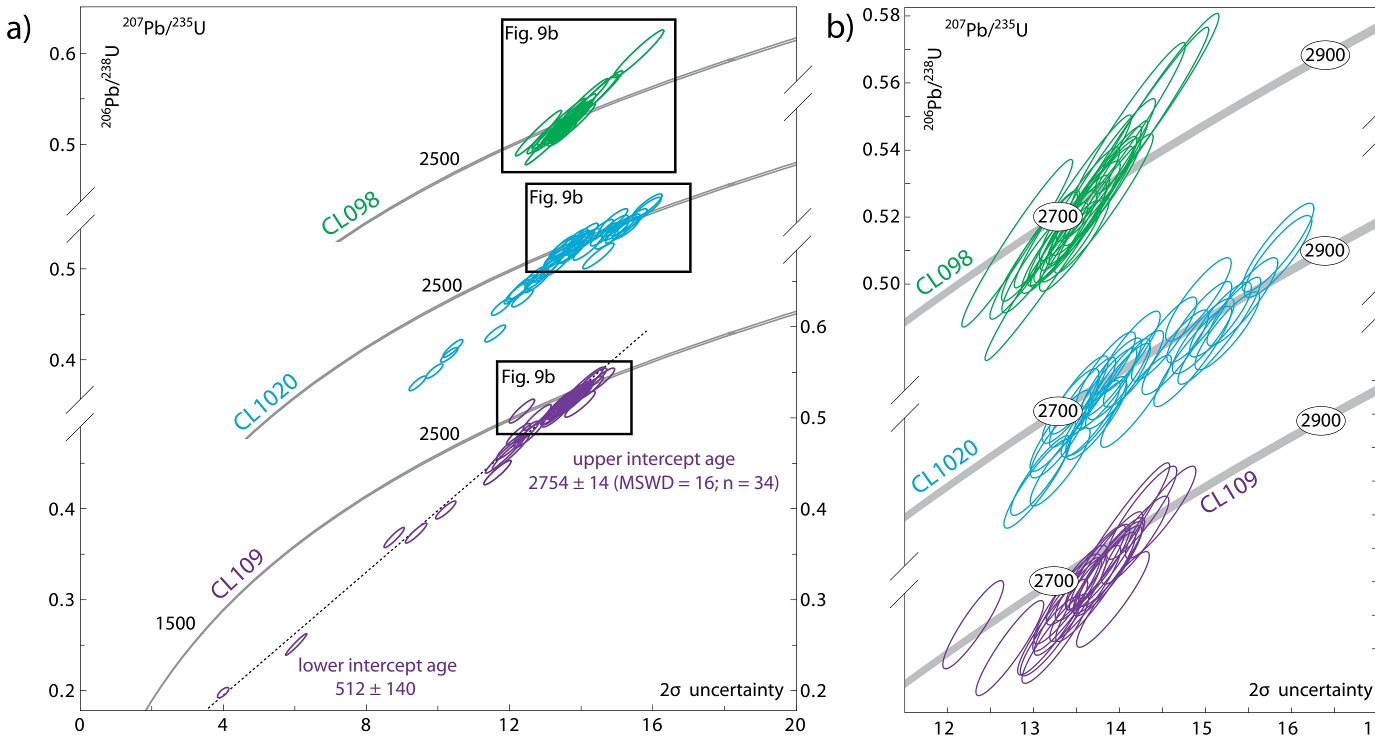

a)
$^{207}Pb/^{235}U$
$^{206}Pb/^{238}U$
Fig. 9b
Fig. 9b
Fig. 9b
2500
2500
2500
1500
CL098
CL1020
CL109
upper intercept age
2754 ± 14 (MSWD = 16; n = 34)
lower intercept age
512 ± 140
2σ uncertainty
b)
$^{207}Pb/^{235}U$
$^{206}Pb/^{238}U$
2700
2900
CL098
CL1020
CL109
2σ uncertainty

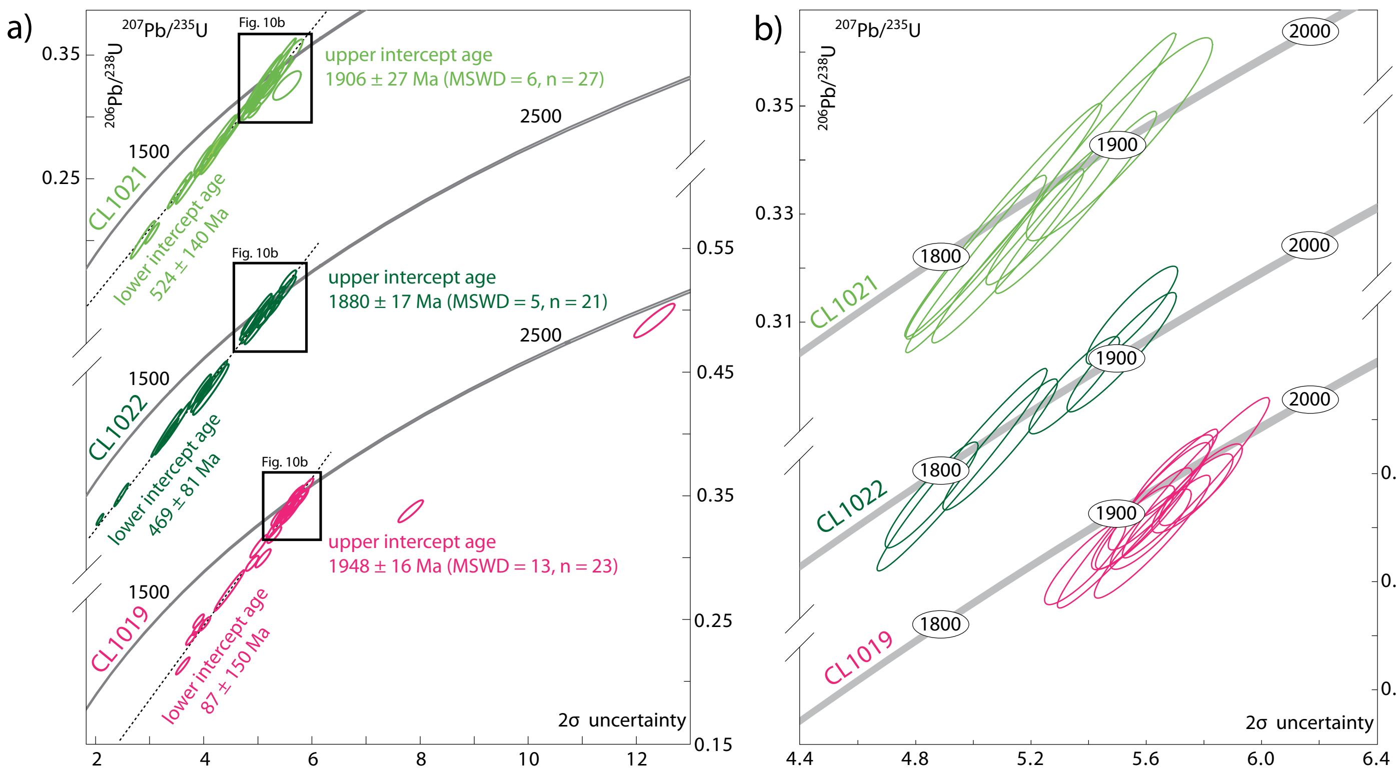

a)
$^{207}Pb/^{235}U$
$^{206}Pb/^{238}U$
Fig. 10b
upper intercept age
1906 ± 27 Ma (MSWD = 6, n = 27)
lower intercept age
524 ± 140 Ma
CL1021
upper intercept age
1880 ± 17 Ma (MSWD = 5, n = 21)
lower intercept age
469 ± 81 Ma
CL1022
upper intercept age
1948 ± 16 Ma (MSWD = 13, n = 23)
lower intercept age
87 ± 150 Ma
CL1019
1500
2500
2σ uncertainty
b)
$^{207}Pb/^{235}U$
$^{206}Pb/^{238}U$
1800
1900
2000
CL1021
CL1022
CL1019
2σ uncertainty

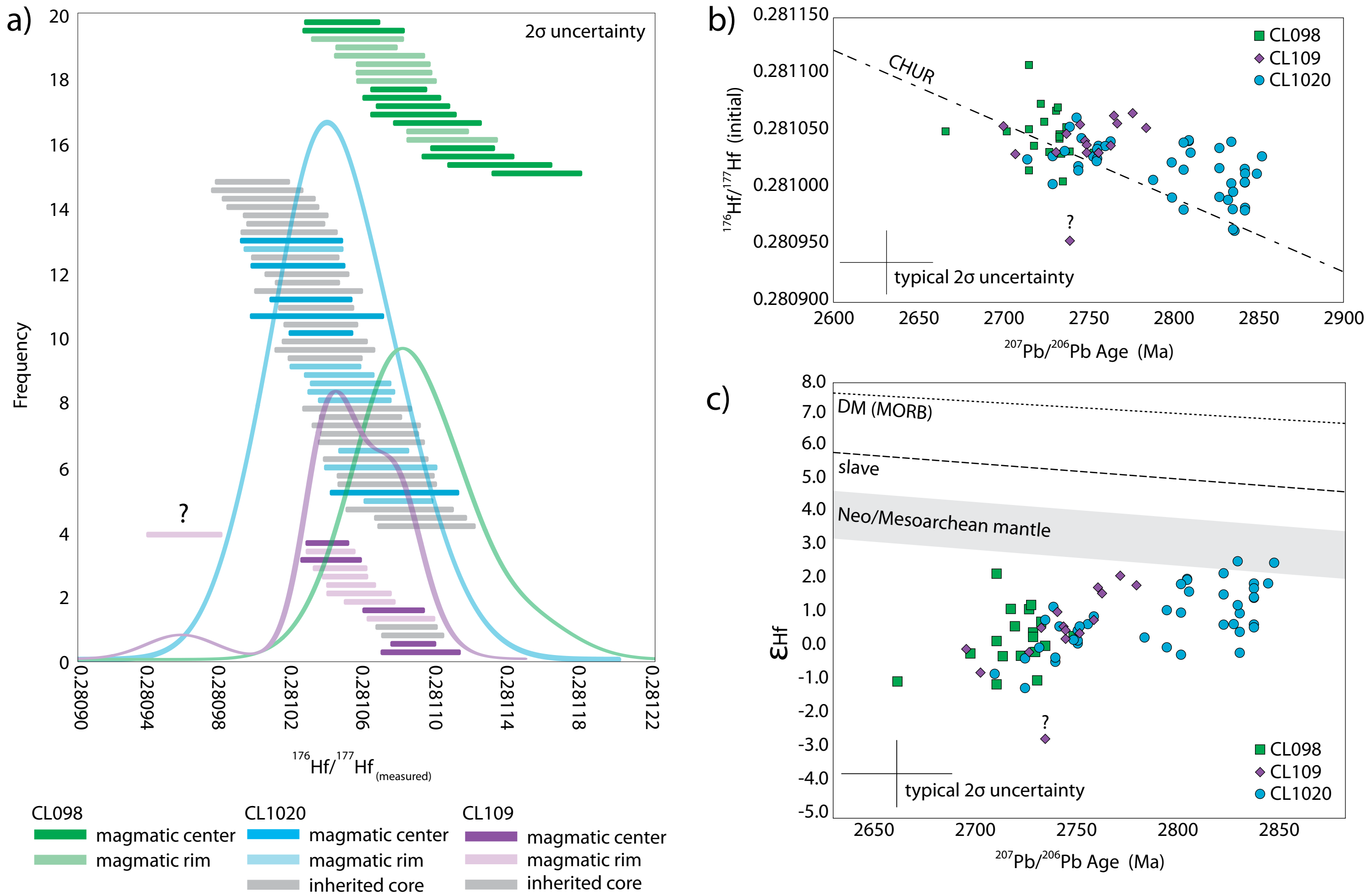

a)
2σ uncertainty
Frequency
?
^{176}Hf/^{177}Hf (measured)
CL098
magmatic center
magmatic rim
CL1020
magmatic center
magmatic rim
inherited core
CL109
magmatic center
magmatic rim
inherited core
b)
CHUR
CL098
CL109
CL1020
^{176}Hf/^{177}Hf (initial)
typical 2σ uncertainty
^{207}Pb/^{206}Pb Age (Ma)
c)
DM (MORB)
slave
Neo/Mesoarchean mantle
εHf
typical 2σ uncertainty
CL098
CL109
CL1020
^{207}Pb/^{206}Pb Age (Ma)

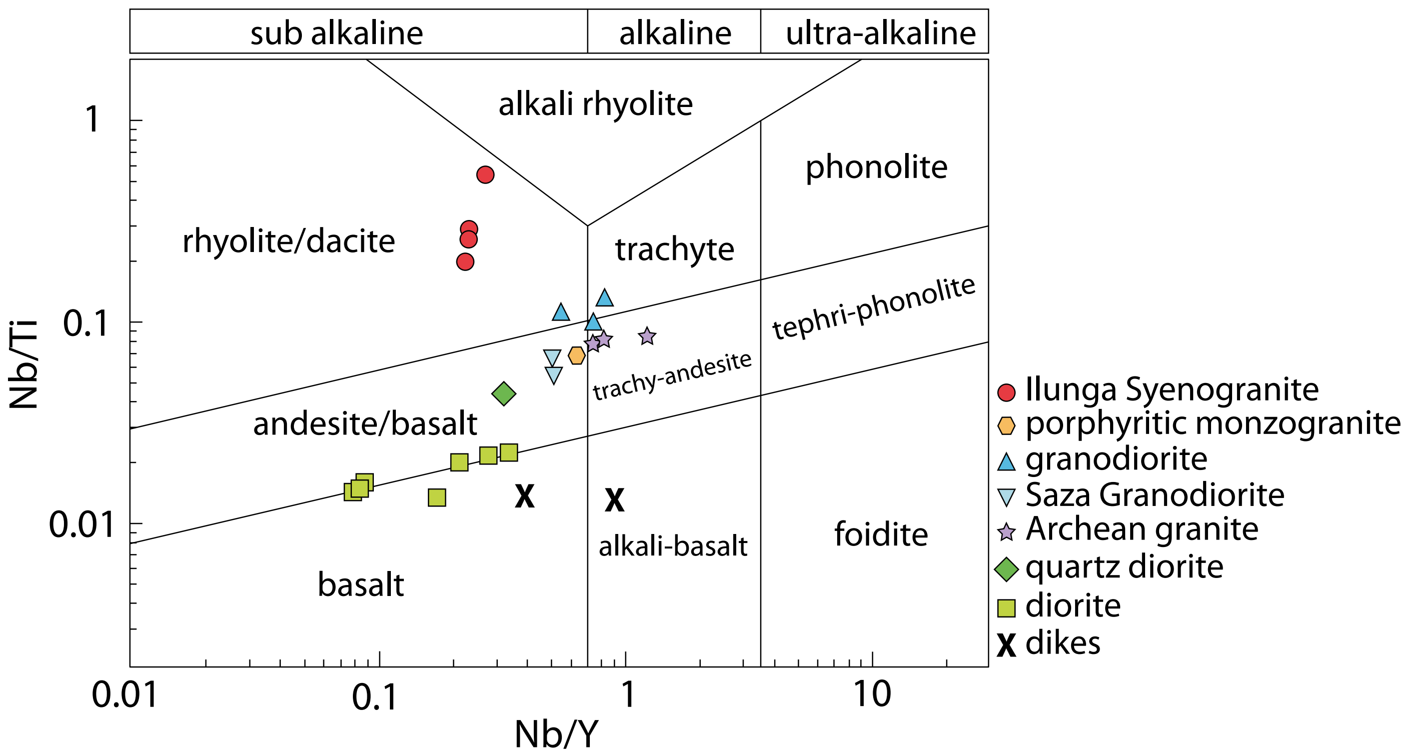
sub alkaline
alkaline
ultra-alkaline
alkali rhyolite
phonolite
rhyolite/dacite
trachyte
tephri-phonolite
trachy-andesite
andesite/basalt
alkali-basalt
foidite
basalt
Nb/Ti
Nb/Y
1
0.1
0.01
10
Ilunga Syenogranite
porphyritic monzogranite
granodiorite
Saza Granodiorite
Archean granite
quartz diorite
diorite
dikes

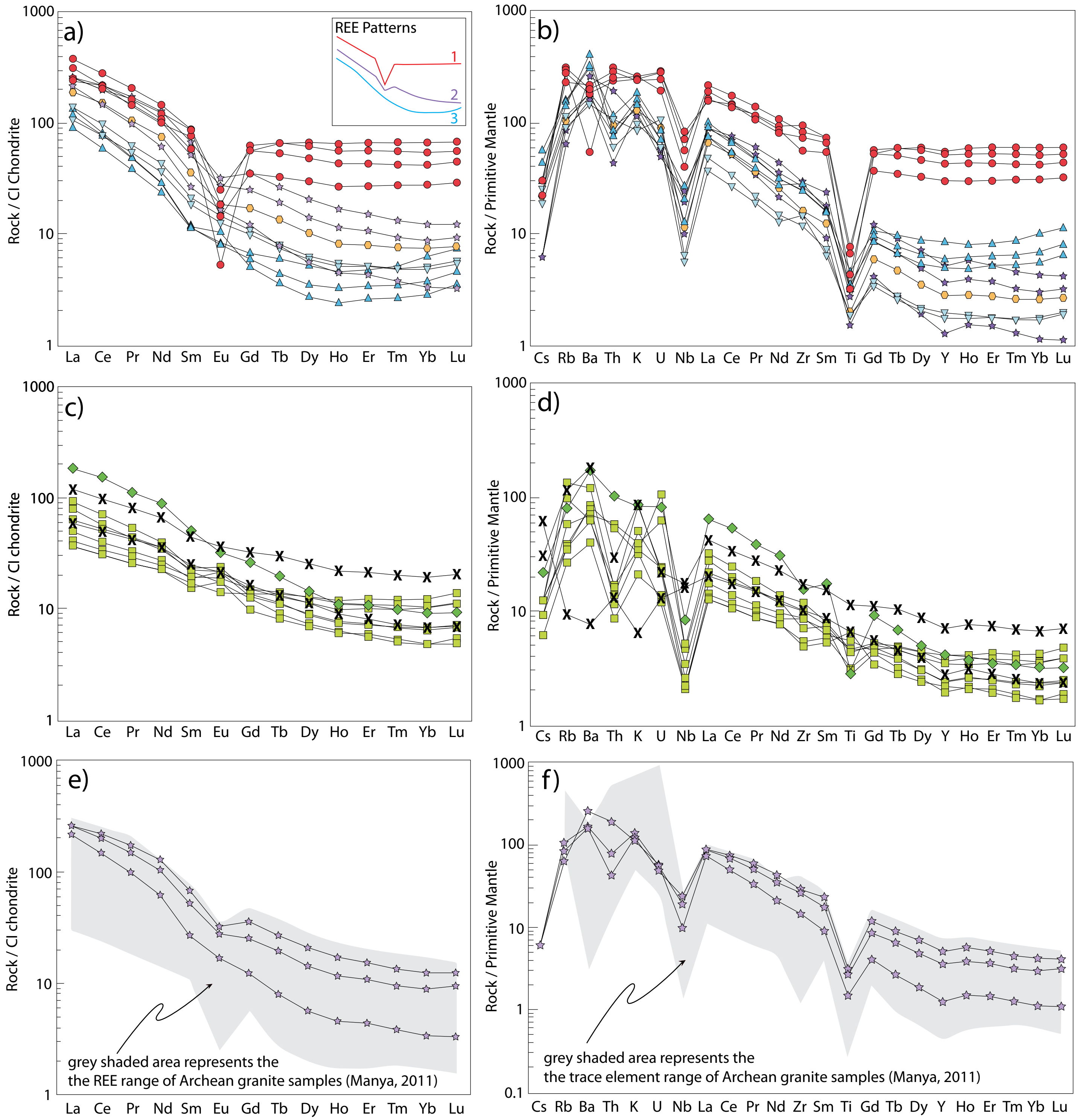
a)
REE Patterns
1
2
3
Rock / CI Chondrite
La Ce Pr Nd Sm Eu Gd Tb Dy Ho Er Tm Yb Lu
b)
Rock / Primitive Mantle
Cs Rb Ba Th K U Nb La Ce Pr Nd Zr Sm Ti Gd Tb Dy Y Ho Er Tm Yb Lu
c)
Rock / CI chondrite
d)
e)
grey shaded area represents the
the REE range of Archean granite samples (Manya, 2011)
f)
grey shaded area represents the
the trace element range of Archean granite samples (Manya, 2011)

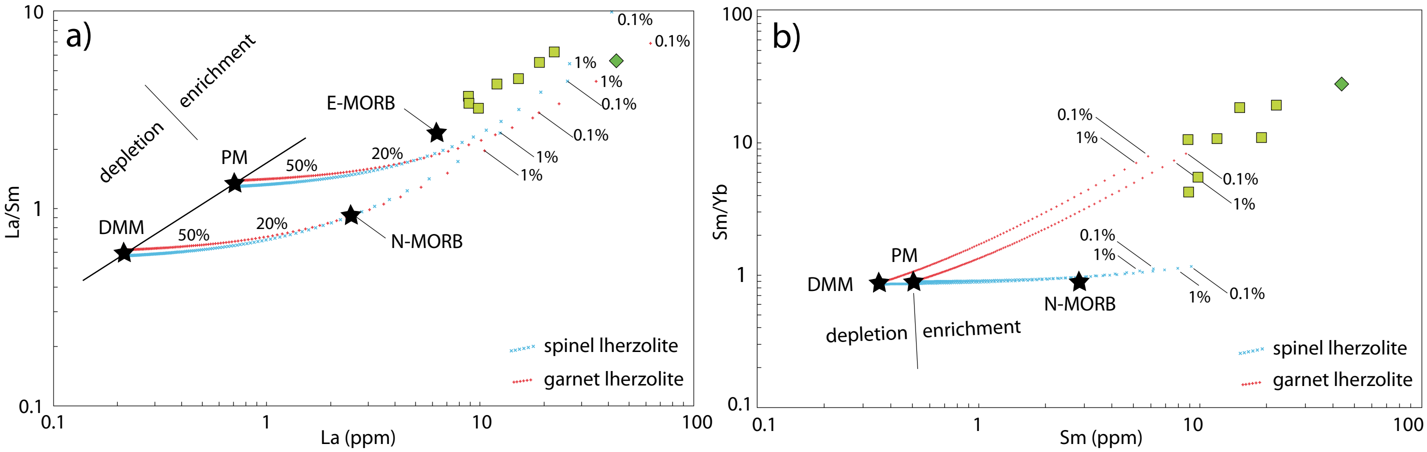

a)
La/Sm
La (ppm)
depletion
enrichment
DMM
PM
E-MORB
N-MORB
50%
20%
1%
0.1%
spinel lherzolite
garnet lherzolite
b)
Sm/Yb
Sm (ppm)
DMM
PM
N-MORB
depletion
enrichment
0.1%
1%
spinel lherzolite
garnet lherzolite

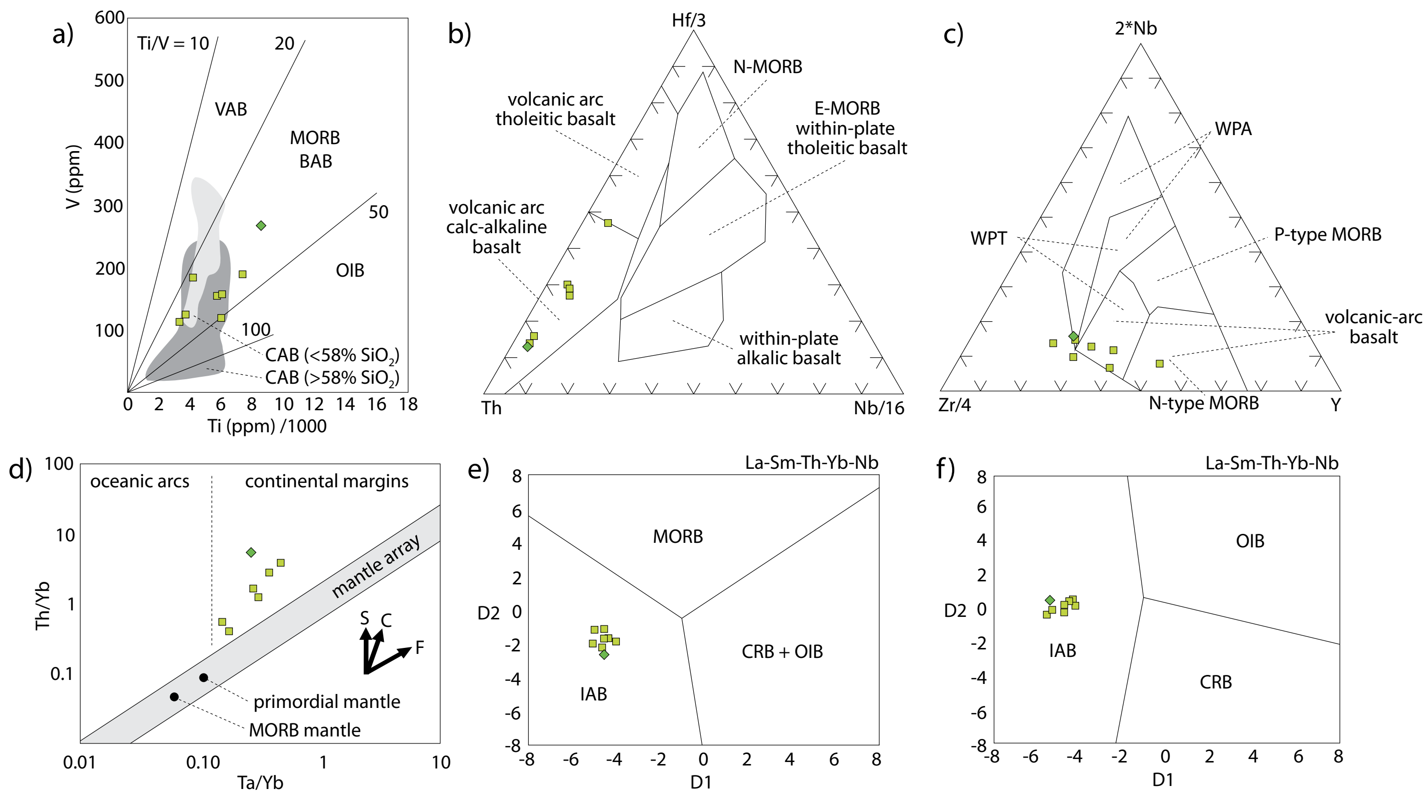
a)
Ti/V = 10
20
50
100
VAB
MORB
BAB
OIB
CAB (<58% SiO2)
CAB (>58% SiO2)
V (ppm)
Ti (ppm) /1000
b)
Hf/3
Th
Nb/16
N-MORB
volcanic arc
tholeitic basalt
E-MORB
within-plate
tholeitic basalt
volcanic arc
calc-alkaline
basalt
within-plate
alkalic basalt
c)
2*Nb
Zr/4
Y
WPA
WPT
P-type MORB
volcanic-arc
basalt
N-type MORB
d)
oceanic arcs
continental margins
mantle array
Th/Yb
Ta/Yb
S
C
F
primordial mantle
MORB mantle
e)
La-Sm-Th-Yb-Nb
MORB
CRB + OIB
IAB
D2
D1
f)
La-Sm-Th-Yb-Nb
OIB
IAB
CRB
D2
D1